Improving Virtual Impactor Performance via Nozzle Optimization

A THESIS
SUBMITTED TO THE FACULTY OF THE GRADUATE SCHOOL
OF THE UNIVERSITY OF MINNESOTA
BY

Mckenna Relling

IN PARTIAL FULFILLMENT OF THE
REQUIREMENTS FOR THE DEGREE OF
MASTER OF SCIENCE

Professor Christopher J. Hogan Jr., Adviser
May 2023

ACKNOWLEDGEMENTS

Thank you to Chris Hogan, who is the best advisor I could have asked for. He has been exceptionally kind, supportive, and encouraging throughout my education. To Stephanie Eilts, who has been an incredible mentor to me and helped me too many times to count. To Tomoya Tamadate, who taught me how to use OpenFOAM and particle simulations and knew the answer to every troubleshooting question I ever had.

I have been so lucky to learn about virtual impactors from a legend in the field, Bernard Olson, who has dedicated extensive time to supporting my work. The entire Hogan lab group stands out in their thoughtfulness and dedication to helping one another.

Lastly, thank you to my wonderful friends and family who have encouraged me every step along the way.

ABSTRACT

Virtual impactors are aerosol-concentrating devices composed of a nozzle and downstream receiving tube. The majority aerosol flow accelerated through the nozzle is diverted from transmitting through the receiving tube, yet particles inertially maintain trajectory into the tube, thereby increasing their concentrations. This study investigated the effect of nozzle geometry on particle focusing, a phenomenon wherein particles not only inertially enter the receiving tube but are radially confined to center streamlines. Specifically, the study aimed to understand how modifications to the nozzle's geometry can improve particle focusing. For this purpose, around 300 nozzles were simulated, with both fluid flow and particle trajectories modeled. The extent of focusing was quantified via a score metric determined by the fraction of particles confined to the inner 10% of the nozzle exit. The study found that shorter nozzles and simple geometries, such as those with a ratio of inlet radius to radius of curvature of around two, tend to have higher scores for particle focusing. The study also suggested the development of a two-stage nozzle to focus larger and smaller particles separately but concluded that the two stages cannot be selected independently of each other. It is suggested that the addition of a straight section between the two stages may allow for independent selection. Two focusing-optimized virtual impactor geometries were experimentally tested and compared to a reference geometry not optimized for focusing. All three impactor geometries were also simulated, and their penetration curves were compared to experimental data. Experimental data points were found to match well with their simulated curves, indicating accurate predictions of impactor performance. One of the optimized geometries showed slightly

worse performance at small particle diameters, but no overfocusing at larger particle diameters, when compared to the reference geometry. The other optimized geometry showed similar performance at small particle diameters, but significantly improved penetration at larger particle diameters. Comparing the overfocusing via the receiving tube collection efficiencies, the two optimized virtual impactors showed 60% and 80% reductions in receiving tube losses, indicating improved particle focusing. The study concludes that the trajectory of particles can be controlled solely via the modification of nozzle geometry, which can be used in conjunction with a virtual impactor to improve the overall ability of the impactor to concentrate particles.

Variable Dictionary

A_1, A_2, A_3	Constants for the Cunningham slip correction factor (2.514,0.8, and 0.5, respectively)
Br	Correlation parameter to bridge the general physics-based drag correlation to the free-molecular expression
C_0	Drag coefficient on the effective sphere
C_1	The scaling for the contribution of the pressure changes across a curved shock
C_c	Cunningham slip correction factor
$C_d, C_{d,SM}, C_{d,Singh}$	Drag coefficient, SM: Stokes-Millikan, Singh
C_d^c	Compressible drag coefficient
$C_{d,fm}$	Drag coefficient for the free molecular regime
C_d^M	Drag coefficient in the hypersonic, continuum limit (=0.9)
d_p	Particle diameter (m)
e	Elementary charge (1.6×10^{-19})
F_d	Drag force acting on a particle (N)
f_{Kn,W_r}	Rarefaction correction to continuum drag coefficient
k	Turbulent kinetic energy density ($m^2\ s^{-2}$)
k_b	Boltzmann's constant ($1.38 \times 10^{-23}\ J\ K^{-1}$)
Kn	Knudson number
M	Mach number
M_s	Post-shock Mach number
m_p, m_g	Mass of gas and particle (kg)
p	Pressure (Pa)
P	Penetration to the minor flow
Re	Reynold's number
t	Time (s)
T	Fluid temperature (K)
T_p	Particle temperature (K)
T_s	Post-shock temperature (K)

T_{Suth}	Reference temperature in Sutherland's equation (K)
U	Particle-gas relative velocity ($m\ s^{-1}$)
U_s	Post-shock gas-particle relative velocity ($m\ s^{-1}$)
u_g	Gas velocity ($m\ s^{-1}$)
v_p	Particle velocity ($m\ s^{-1}$)
W_r	Rarefaction parameter
W_r^T	The ratio of the nonlinear to linear constitutive relations
α	Mapping function to approximate effects of hyperbolic structure of the shock
α_0	Shock curvature parameter (=0.356)
α_{hoc}	High speed rarefaction correction (=1.27)
γ	Ratio of specific heat capacities
d_0	Boundary layer thickness scaling (=9.4)
η	Bridging function modulator (=1.8)
λ	Particle mean free path (m)
μ	Gas viscosity (Pa s)
Θ	The ratio of stagnation pressure and local pressure
ρ_g	Gas density (kg m^{-3})
ρ_g	Particle density (=1000 kg m^{-3})
ω	Specific dissipation rate
ς	Modification factor due to the variation of viscosities across the shock

TABLE OF CONTENTS

LIST OF FIGURES

CHAPTER 1: INTRODUCTION

Inertial separation is a technique commonly used to control the behavior of and collect or concentrate aerosol particles. In an inertial separation device, the effects of the fluid flow dominate the trajectory of smaller particles, while inertial effects dominate the trajectory of larger particles (Qi & Liu, 2021). The introduction of a sudden bend in the fluid flow creates a divide between particles which have sufficient momentum to break away from the fluid streamlines and continue their inertia-driven trajectory, and the particles that will follow streamlines. The critical size at which this divide occurs is known as the cut-point and is a function of the geometry of the separation device, as well as the relative velocity between the particle and fluid (Lin & Heintzenberg, 1995). There are many aerosol devices which employ the physics of inertial separation, from impingers and dust counters to cascade and virtual impactors (Hinds, 1999). Often, these devices consist of particle-laden air directed at a flat plate, which particles will either flow around or impact upon, depending on the critical particle diameter of the system. For applications in which it is desirous to do something with the particles after sampling, a receiving tube replaces the flat plate, and a small flow carries particles out of the tube. The air in the tube is close to stagnant, creating what is known as a virtual impaction surface. (Marple, 2004).

For the applications of sampling and concentration, virtual impactors are one of the most widely used inertial separation devices. In a virtual impactor, the larger portion of the airstream, which the smaller particles follow, is known as the major flow, whereas

the smaller portion of the flow into the receiving tube, which the larger particles enter, is known as the minor flow. (Marple & Chien, 1980).

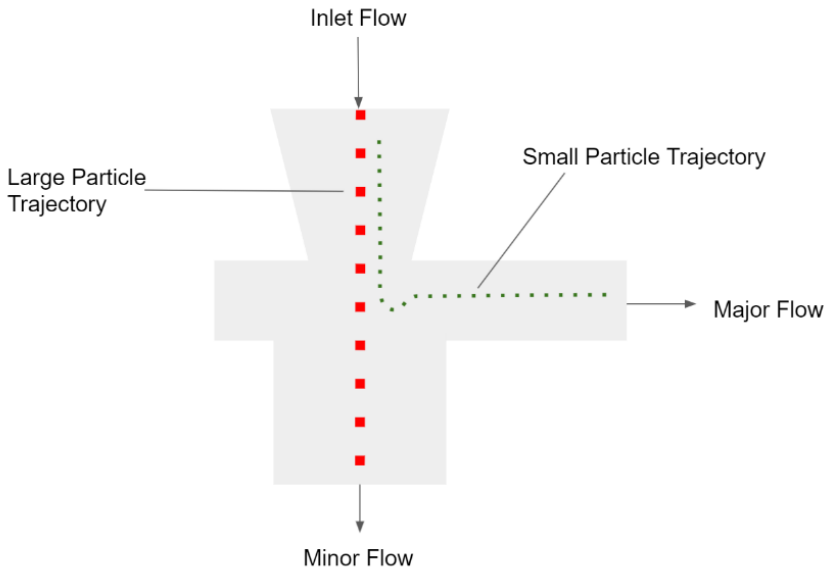

Figure 1. A diagram depicting the particle trajectories within a virtual impactor. High inertia particles travel straight, while the smaller particles follow streamlines.

The critical number that governs inertial behavior in a virtual impactor is Stokes number, and is a function of particle mass, gas velocity, nozzle diameter, and friction factor (Israel & Rosner, 1982). The critical Stokes number translates to a critical particle diameter for a fixed flow rate, traditionally called the cut point, and is defined as the size at which 50% of particles are collected. Below the critical Stokes number particles will never impact and above the critical Stokes number particles will always impact (Sioutas, Koutrakis, & Olson, 1994). In virtual impactors, the Stokes number can be exploited by modifying nozzle geometries to change impactor performance. Thus, virtual impactors are a useful tool for improved concentration across a wide range of applications, since their cut point can be varied based on the desired size range of particles to be

concentrated. The concentration factor of particles above the critical diameter into the minor flow is the ratio of the sample flow rate to the minor flow rate and is typically 10:1. For the highest possible concentration factor, it is desirable to maximize the collection efficiency into the minor flow, while minimizing the collection efficiency in all other possible regions of deposition, which are considered losses. One common reason for particle losses is overfocusing (radial inertial motion leading to deposition) within the nozzle and major flow chamber (Eilts et al, 2021). The overfocusing phenomenon limits the upper size range of particles that can be concentrated, particularly at high Reynolds numbers.

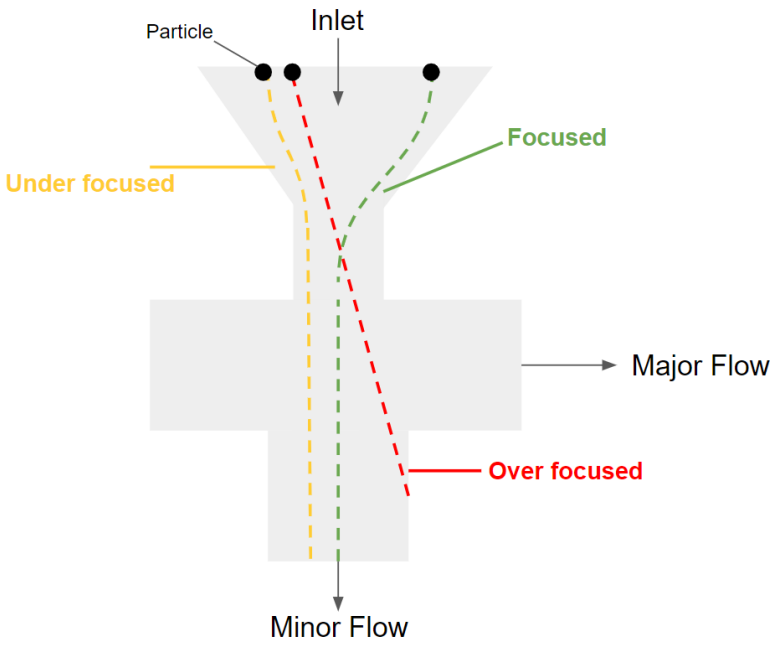

Figure 2. Depiction of under-focused, focused, and over-focused particle trajectories within a virtual impactor.

Another option for the effective sampling and concentration of particles is an aerodynamic focusing lens. Aerodynamic focusing lenses typically consist of a series of

orifices of decreasing sizes through which a dilute aerosol passes. Each orifice focuses an increasingly small particle size to the centerline of the nozzle, resulting in a narrow beam. Thus, the gas flow away from the centerline becomes virtually free of particles and the overall concentration of particles per unit volume increases (Schreiner, 1998). These aerodynamic focusing lenses typically operate at low pressure, as atmospheric pressure lenses are limited by turbulent transition at higher flow rates and larger orifice dimensions leading to turbulent dispersion (Novosselov, 2017). Specifically, the focusing capability of an aerosol focusing lens will quickly decrease at Reynolds numbers larger than 70 (Eichler et. al, 1998). For focusing to occur at ambient conditions while remaining laminar, the flow rate through the nozzle would be so low that it would no longer be compatible with most aerosol air sampling instruments, nor would it be able to sample sufficient particles within a reasonable timeframe.

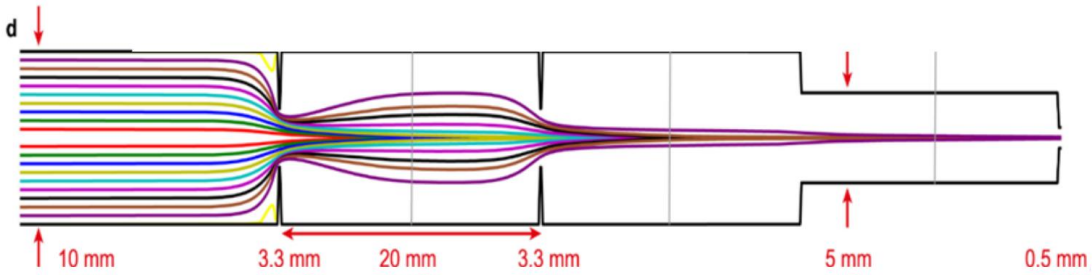

Figure 3. Aerodynamic focusing lens with series of contractions leading to particle focusing. Figure modified and reprinted with permission from Roth et. al (2018). Journal of Aerosol Science, Volume 124, 2018, Pages 17-29, ISSN 0021-8502, https://doi.org/10.1016/j.jaerosci.2018.06.010.

For highly effective sampling, it would be powerful to combine both a virtual impactor and a focusing nozzle. A focused beam would allow for a reduction in the size of the receiving tube, thus increasing the ratio of total flow rate to minor flow rate and increasing the overall concentration factor by the same ratio (Fuerstenau, 1994). Furthermore, a focused nozzle would reduce the surfaces losses within the impactor that result from the overfocusing of particles. Although the combination of a virtual impactor and focusing nozzle is promising, its accomplishment is not a trivial feat to construct. To create a focusing nozzle that effectively concentrates particles of a wide variety of sizes is a careful balance, as an abrupt contraction in geometry is desirable for focusing particles, but a smooth contraction is necessary to maintain a stable flow configuration (Vidal-de-Miguel & de la Mora, 2012). Furthermore, the higher velocities needed to focus smaller particles can lead to negative radial effects on larger particles, promoting overfocusing. Thus, effective inertial particle control requires a multi-dimensional consideration of the forces at work.

Due to these challenges, the combination of inertial separation and focusing is sparingly studied in the literature. For lab-on-a-chip applications, inertial particle focusing has been achieved in curved channels that have shown focusing within 19% of the channel width (Ying and Lin, 2019). However, the particle size range in these applications is not wide, as the maximum Reynolds number in the microchannels of approximately 100 is not sufficient to focus small particles. Furthermore, these studies do not involve the increased concentration of particles for sampling. Mahdavipour et al (2019) combined a virtual impactor with a groove-induced envelope flow particulate matter focusing system, which resulted in an improved collection efficiency of airborne

particulates. Problems with this system included a high cut-point of 2.5 μm, which is higher than desired by many sampling applications. Additionally, this impactor was for a microfluidic application and used a sheath flow for focusing. Woo et al., (2019) proposed a concept for a focusing device for submicrometer particle concentration at ambient pressure, which could enhance the size range of a virtual impactor. However, the particle focusing was achieved via electrical, not inertial, methods.

The most relevant study regarding virtual impaction and focusing comes from Vidal-de-Miguel & Fernandez de la Mora (2012), who studied the theoretical combination of a focusing nozzle and virtual impactor and numerically analyzed a three-contraction focusing nozzle. Limitations of the study included the use of an incompressible flow model and the simplification of independence between the contractions. Furthermore, the development of the focusing nozzle was based on an iterative numerical approach, and no experimental work was performed.

This study seeks to optimize the focusing of particles in combination with a virtual impactor, creating a powerful tool for inertial particle control and sampling. In this thesis, nearly 300 single stage focusing nozzles were designed and simulated. A scoring system was devised to parametrize the focusing capabilities of each nozzle. Two of the best nozzles were built into a virtual impactor and tested, then compared to a previously studied nozzle to demonstrate improved particle concentration. Two-stage nozzles were also simulated and their focusing capabilities were studied. Lastly, the experimental results of focusing virtual impactors were compared to simulations.

CHAPTER 2: METHODS

2.1 Simulation Methods

2.1.1 Geometry Definition

The geometry of each single-stage nozzle can be defined by five parameters: inlet length, nozzle length, nozzle radius, inlet angle theta, and radius of curvature. Of these parameters, nozzle length and nozzle radius were held constant while the others were varied. Figure 4 shows these parameters, with the varied parameters indicated in red.

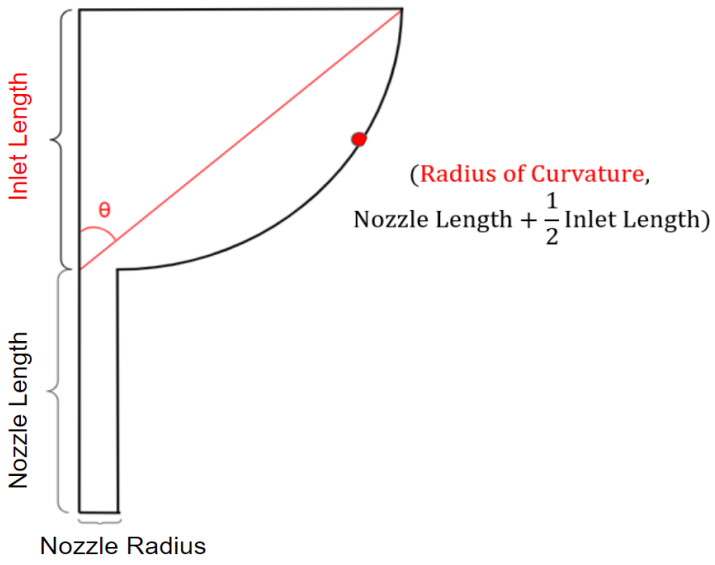

Figure 4. Single-stage geometry parameters. The inlet length, angle, and radius of curvature were varied for each simulation.

Theta varied between 20 degrees and 80 degrees, in increments of 10 degrees. The inlet length was either 1, 5, 10, 15, or 20 mm. The radius of curvature was varied as

ten evenly spaced values between the nozzle radius and the inlet radius. The geometry of every combination of these values was constructed, with some omitted due to having an unreasonable structure. This resulted in 289 total nozzle geometries.

2.1.2 Computational Fluid Dynamics

Computational fluid dynamics (CFD) simulations were performed for every nozzle using OpenFOAM-v2012 with a compressible, steady form of the continuity equation, the Navier-Stokes equation, and the energy equation (Gatski & Bonnet, 2009).

The continuity equation can be written as the following:

$$\frac{d\rho}{dt} + \frac{d}{dx_j}\left[pu_j\right] = 0 \tag{1}$$

The momentum equation is:

$$\frac{d}{dt}(\rho u_i) + \frac{d}{dx_j}\left[\rho u_i u_j + p d_{ij} - \tau_{ij}\right] = 0 \tag{2}$$

And the energy equation is:

$$\frac{d}{dt}(\rho e_0) + \frac{d}{dx_j}\left[\rho e_0 u_j + p u_j + q_j - u_i \tau_{ij}\right] = 0 \tag{3}$$

Assuming Stokes law and a Newtonian fluid, the viscous stress is given by:

$$\tau_{ij} = 2\mu S_{ij}^{*} \tag{4}$$

The trace-less viscous strain-rate is given by:

$$S_{ij}^{*} \equiv \frac{1}{2}\left(\frac{du_i}{dx_j} + \frac{du_j}{dx_i}\right) - \frac{1}{3}\frac{du_k}{dx_k} d_{ij} \tag{5}$$

The heat flux, q_j, is given by Fourier's law:

$$q_j = -\lambda \frac{dT}{dx_j} \equiv \frac{-C_p \mu}{Pr} \frac{dT}{dx_j} \tag{6}$$

The laminar Prandtl number is defined as:

$$Pr \equiv \frac{C_p \mu}{\lambda} \tag{7}$$

It is assumed that the fluid is a calorically perfect gas to close these equations (constant specific heat).

Finally, the total energy is given as:

$$e_0 \equiv C_v T + \frac{u_k u_k}{2} \tag{8}$$

The SIMPLE (Semi-Implicit Method for Pressure-Linked Equations) algorithm was used to solve these equations (Patankar & Spalding, 1972). The Favre-averaged versions of these equations were used for the actual solution since the instantaneous equations cannot be solved. The flow was assumed to be laminar and an ideal gas with a molar mass of 28.9 g mole^{-1}. The viscosity of the flow was calculated using the Sutherland equation. The pressure, temperature, and velocity fields were solved using an axis-symmetric model.

At the inlet, the boundary conditions were a temperature of 300 K, a prescribed mass flow rate, and no pressure gradient. At the outlet, the boundary conditions were no gradient in temperature or velocity and a pressure of 0.68 atm. The outlet pressure was selected to match the pressure condition of the major flow cavity for when the nozzle is used in conjunction with a virtual impactor design. A sample mesh used for a single-stage nozzle, along with boundary conditions, is depicted in Figure 2.

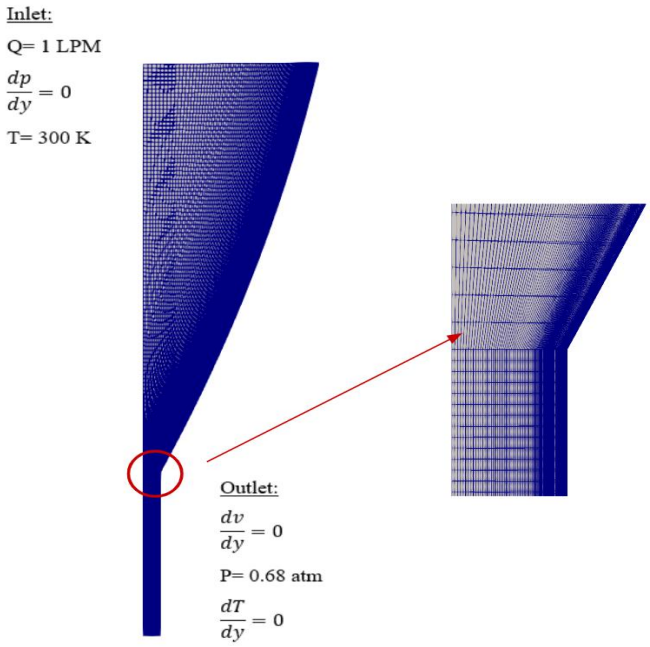

Figure 5. Single-stage boundary conditions and mesh.

2.1.3 Particle Trajectory Calculations

Using the results from the pressure, temperature, and velocity calculations, the particle trajectories were calculating using a custom C++ code written by Dr. Tomoya Tamadate. The governing equation for these trajectories is Newton's First Law, with the only significant force acting on the particle being the force due to drag:

$$m_p \frac{d\overrightarrow{v_p}}{dt} = |F_d| \frac{\left(\overrightarrow{u_g} - \overrightarrow{v_p}\right)}{\left|\overrightarrow{u_g} - \overrightarrow{v_p}\right|} \tag{9}$$

$|F_d|$ is the magnitude of the drag force, $\overrightarrow{v_p}$ is the particle velocity vector, $\overrightarrow{u_g}$ is the gas velocity vector, m_p is the mass of the particle, and t is time. The drag force is the typical expression for the drag on a spherical particle:

$$|F_d| = \frac{1}{2}\rho_g U^2 C_d \left(\frac{\pi d_p^2}{4}\right) \tag{10}$$

where ρ_g is the density of the fluid, U is the relative velocity between the particle and fluid, defined as $\left|\overrightarrow{u_g} - \overrightarrow{v_p}\right|$, and C_d is the drag coefficient. Typically, the Stokes-Millikan relationship is used to define the drag coefficient:

$$C_{d,SM} = \frac{1}{C_c}\frac{24}{Re} \tag{11}$$

$$C_c = 1 + Kn\left[A_1 + A_2 e^{-\frac{A_3}{Kn}}\right] \tag{12}$$

Re is the particle Reynolds number $\frac{\rho_g U d_p}{\mu}$ and C_c is the Cunningham slip correction factor with constants $A_1 = 2.514$, $A_2 = 0.8$, and $A_3 = 0.55$. Kn is the Knudsen number, defined as the ratio of the mean free path of the fluid to the diameter of a particle. Although this drag coefficient is accurate across a wide range of Knudsen numbers, the requirements for the Stokes-Millikan relationship are not always valid for nozzles approaching the sonic flow limit. Therefore, the particle trajectory calculations in this study used the more recently developed Singh drag model (Singh et al, 2021), which are valid across a substantially wider range of particle Reynolds and Knudsen numbers. This more complex drag coefficient can be described by the following series of equations:

$$C_{d,Singh} = C_d^c f_{Kn,W_r}\frac{1}{1+Br^\eta} + C_{d,fm}\frac{Br^\eta}{1+Br^\eta} \tag{13a}$$

$$Br = W_r^T\frac{M^{2\varsigma-1}+1}{M^{2\varsigma-1}} \tag{13b}$$

$$W_r^T = \frac{M^{2\varsigma}}{Re}\left(1+\frac{T}{T_s}\right)^\varsigma \tag{13c}$$

$$f_{Kn,W_r} = \frac{1}{C_c}\frac{1}{1+\alpha_{hoc}W_r^T} \tag{13d}$$

$$C_{d,fm} = \frac{(1+2s^2)\exp(-s^2)}{s^3\sqrt{\pi}} + \frac{(4s^4+4s^2-1)\,\mathrm{erf}(s)}{s^3\sqrt{\pi}} + \frac{2}{3s}\sqrt{\pi\frac{T_p}{T}} \tag{13e}$$

$$s = M\sqrt{\frac{\gamma}{2}} \tag{13f}$$

$$C_d^c = C_1\left(1-\alpha\frac{U_s}{U}\right) + C_o\Theta\left(1+\alpha\frac{\delta_0}{\widetilde{Re}_s^{0.5}}\right) \tag{13g}$$

$$\Theta = \left[1+(\gamma-1)\frac{M_s^2}{2}\right]^{\frac{\gamma}{\gamma-1}} \tag{13h}$$

$$\widetilde{Re}_s = Re\left(\frac{1}{\alpha^2}\frac{T}{T_s}\right)^{\varsigma}\Theta^{\left(\gamma+\frac{1}{2\gamma}\right)-\left(\frac{\gamma-1}{\gamma}\right)\varsigma} \tag{13i}$$

$$\alpha = \frac{1}{\alpha_0 M + 1 - \alpha_0} \tag{13j}$$

When M<1

$$\frac{T_s}{T} = 1 \tag{13k}$$

$$\frac{U_s}{U} = 1 \tag{13l}$$

$$M_s = M \tag{13m}$$

$$\alpha = 1 \tag{13n}$$

$$C_1 = 1 \tag{13o}$$

When M≥1

$$\frac{T_s}{T} = \frac{[(\gamma-1)M^2+2][2\gamma M^2-(\gamma-1)]}{(\gamma-1)^2M^2} \tag{13p}$$

$$\frac{U_s}{U} = \frac{(\gamma-1)M^2+2}{(\gamma+1)^2M^2} \tag{13q}$$

$$M_s = \sqrt{\frac{(\gamma-1)M^2+2}{2\gamma M^2-(\gamma-1)}} \tag{13r}$$

$$\alpha = \frac{1}{\alpha_0 M + 1 - \alpha_0} \tag{13s}$$

$$C_1 = \frac{C_d^M - C_0\left\{1+\left[\frac{(\gamma-1)^2}{4\gamma}\right]\right\}^{\frac{\gamma}{\gamma-1}}}{1-\frac{1}{a_0 M}\frac{\gamma-1}{\gamma+1}} \tag{13t}$$

This equation is transcribed in its entirety here due to its importance in accurately modeling the trajectory of particles when dealing with a wide range of Mach and Knudsen numbers. At lower Reynolds numbers (Re<=0.01), the particle trajectories are calculated analytically, and at higher Reynolds numbers (Re>0.01) the particle trajectories are calculated numerically using the Verlet integration method. This hybrid approach allows for a larger time step to be used when the fluid velocity is small and conditions are not changing rapidly, and a smaller time step to be used as particles accelerate through the nozzle. As a result, the calculation time necessary to determine the particle trajectories is dramatically reduced.

For the particle simulations, seven different particle diameters (0.3, 0.5, 1, 3, 5, and 10 μm) were modeled as spheres with unit density (1000 kg m^{-3}). 100 particles of each of the seven different diameters were evenly dispersed radially across the inlet of the nozzle.

To evaluate the effectiveness of each particle at focusing, a scoring system was devised. The score of a nozzle is defined as the following:

$$Score = \frac{A_{focused}}{A_{total}} \frac{\int_{\log(d_{p,lower})}^{\log(d_{p,upper})} P_{foc}\, \partial d_p}{d_{p,upper} - d_{p,lower}} \tag{14}$$

$\frac{A_{focused}}{A_{total}}$ is the desired fractional reduction in area to which particles should be focused, $d_{p,upper}$ and $d_{p,lower}$ are the maximum and minimum particle diameters of interest, respectively, and P_{foc} refers to the fraction of particles which penetrate within $\frac{A_{focused}}{A_{total}}$ of the nozzle exit and is a function of particle size. Integration was performed on a log basis because it allows for each particle size to be weighted evenly. The focused region considered was ten percent of the nozzle area, leading to a maximum score of approximately 1000. The 10% focused region was selected because it was found to be a good balance between a too small region, which would be unrealistic, and a too large region, which would not strongly suggest good focusing.

2.1.4 Mesh Refinement and Simulation Convergence The total number of cells in each mesh was 2.0×10^5. Validation of the mesh was performed by checking that increasing the fineness of the mesh did not significantly change the particle trajectory calculations. The particle trajectories are deterministic and can be parametrized via the scoring system described previously.

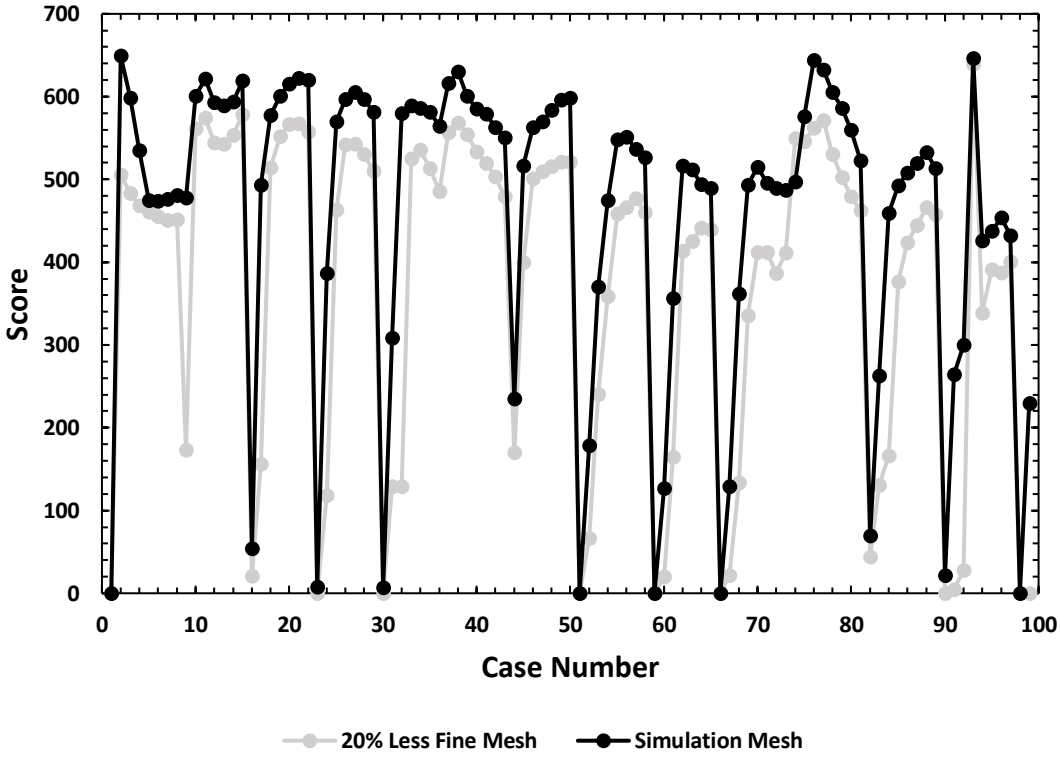

Figure 6. Mesh comparison between the mesh used in the simulation and a 20% less fine mesh. Results are parameterized via a scoring system which is deterministic.

Figure 6 compares the scores of the nozzles used in the simulation mesh to the scores of the same nozzles with a mesh that is 20% less fine, for a sample of 100 nozzles. The offset in scores is consistent, and the relative difference in score between cases is maintained. Overall, neglecting the cases in which the percentage difference is large due to the score being very low, the average difference in score is 12%. Thus, the mesh employed is sufficiently fine to determine the nozzles whose relative performance is greatest.

The simulation ran for 10,000 time-steps at the beginning of each new inlet length. Then, for efficiency, the following geometry would take over the result from the previous geometry and run for an additional 1,000 time-steps. This process would continue for all radius of curvatures and inlet radii within each inlet length, then start again with 10,000 time-steps once the inlet length changed. Below, the graphs show the initial residual axial velocities for a case of 10,000 and a case of 1,000 time-steps. From these graphs, the simulations are well-converged.

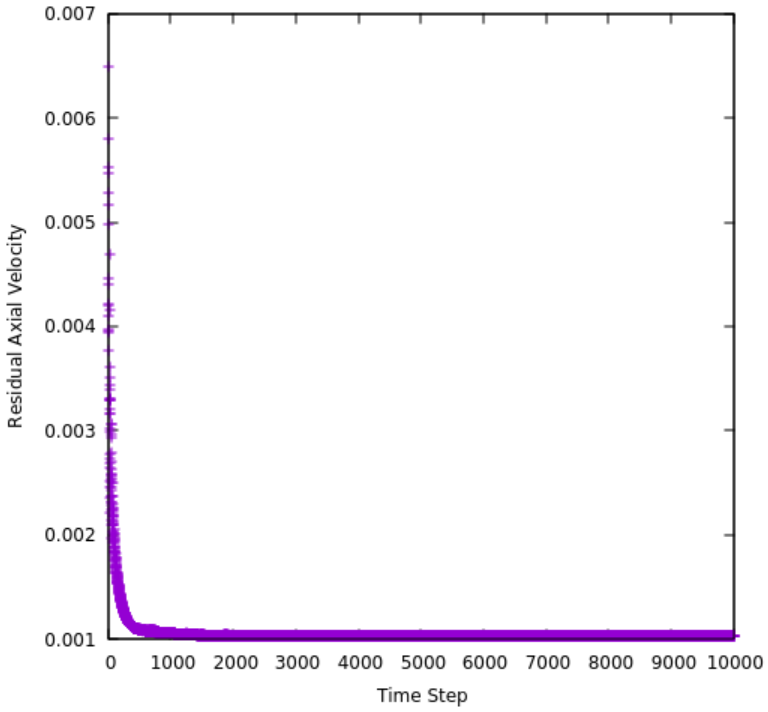

Figure 7. A plot of the axial velocity residuals versus simulation time step for new inlet length case to demonstrate simulation convergence

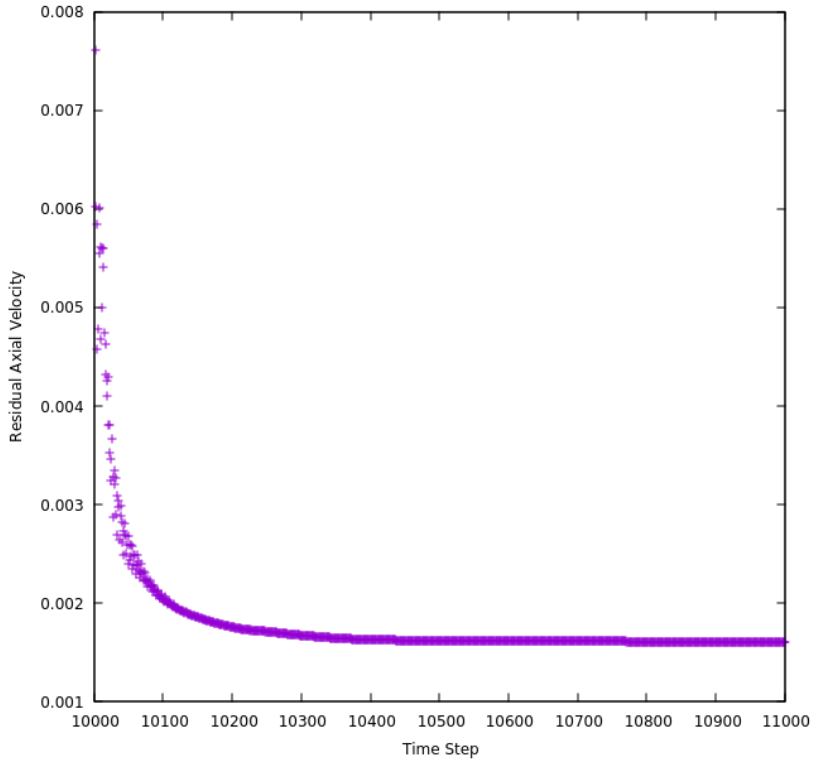

Figure 8. A plot of the axial velocity residuals versus simulation time step after taking on the previous result to demonstrate simulation convergence

2.1.5 Two-Stage Nozzles

A similar procedure was followed for the two-stage nozzles. The geometry of each stage was defined in the same way as the one stage nozzle. The values of the inlet angles ranged in 10-degree increments from 20 degrees to 80 degrees. The values of the radius of curvatures were ten evenly spaced increments between the inlet of that stage and the inlet of the region below. The inlet length was either 1, 5, 10, 15, 20, 25, or 30 mm. In each series of two stage nozzles, the bottom stage was set to be a single-stage nozzle that had a high focusing score, while the upper stage was allowed to vary. Three sets of two-stage nozzles were evaluated, each with a different lower-stage geometry.

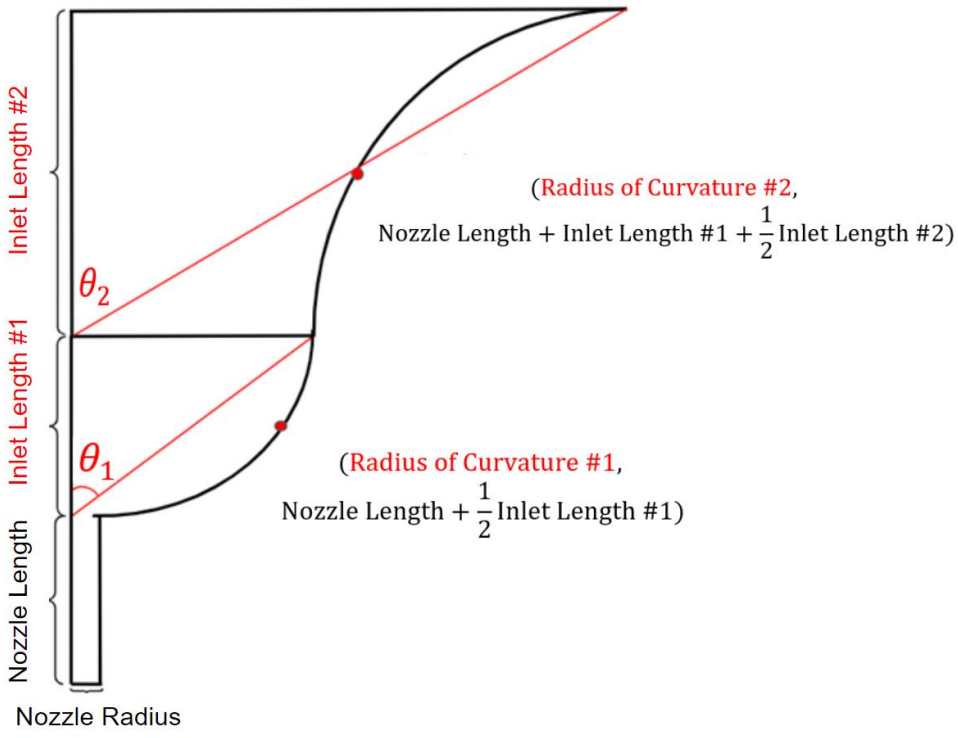

Figure 9. Geometry definition for two stage nozzles. Six parameters were varied for each two stage nozzle: two inlet lengths, two angles, and two radii of curvature.

The CFD and particle trajectory calculation methods for the two stage nozzles were identical to that of the one stage. The mesh used for the two-stage nozzles was identical to that of the one stage. Convergence for the two-stage nozzle simulations can be seen in Figure 10.

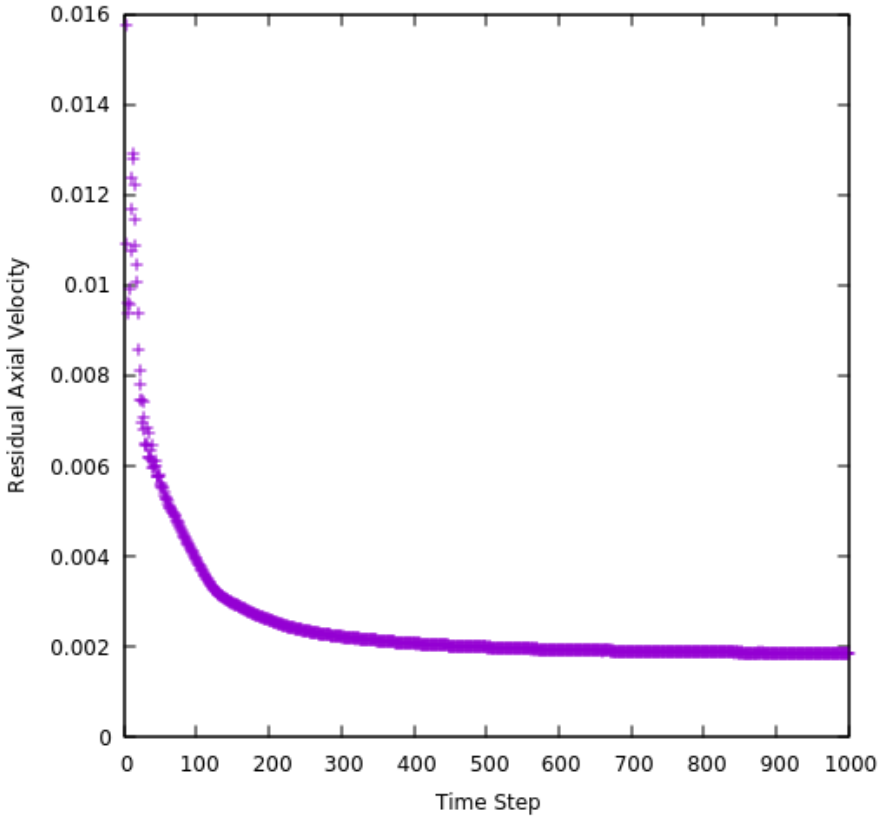

Figure 10. A plot of the axial velocity residuals versus simulation time step demonstrate simulation convergence

2.1.6 Full Impactor Simulations

CFD simulations and particle trajectory simulations were also performed for the three impactor designs that were manufactured and tested. The CFD simulations were nearly identical to the nozzle simulations, except for that the model is adjusted to account for turbulence. While the nozzle simulation can be assumed laminar due to its simple and well-defined nature, the rapid change in flow direction and velocity in the virtual impactor leads to turbulence. In this model, the $k-\omega$ turbulence model used was used to predict the flow behavior.

At the inlet, the boundary conditions were a temperature of 300 K, a prescribed mass flow rate, and atmospheric pressure. For the minor flow, boundary conditions were a mass flow rate 10% of that of the inlet, zero gradient in pressure, and a temperature of 300K. For the major flow, boundary conditions were no gradient in velocity, a pressure of 63.5 kPa, and a temperature of 300K. The mesh used for the full impactor simulation, along with boundary conditions, is depicted in Figure 11.

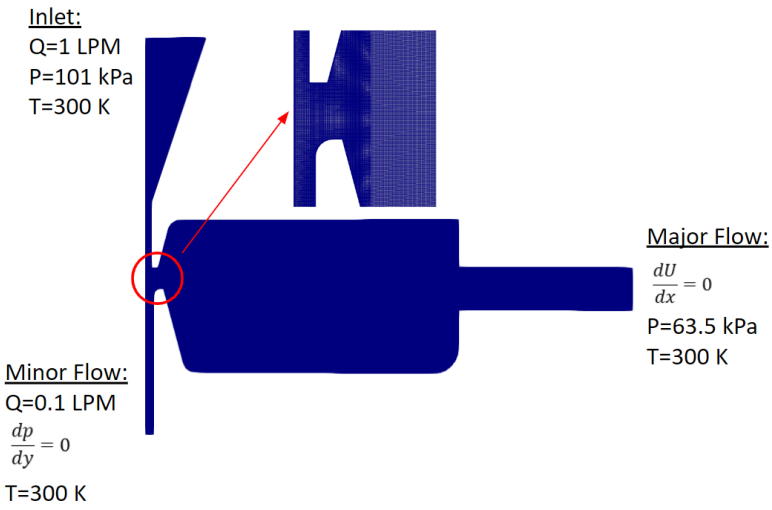

Figure 11. Full impactor boundary conditions and mesh

A mesh refinement study was performed for the full impactor simulations, showing that the penetration of particles into the minor flow, which characterizes the impactor's performance, does not change significantly when the mesh fineness is reduced by 20%. The maximum difference in penetration for the three different impactors which were simulated are 11%, 5%, and 21%, but most points are contained within 5% of the original mesh.

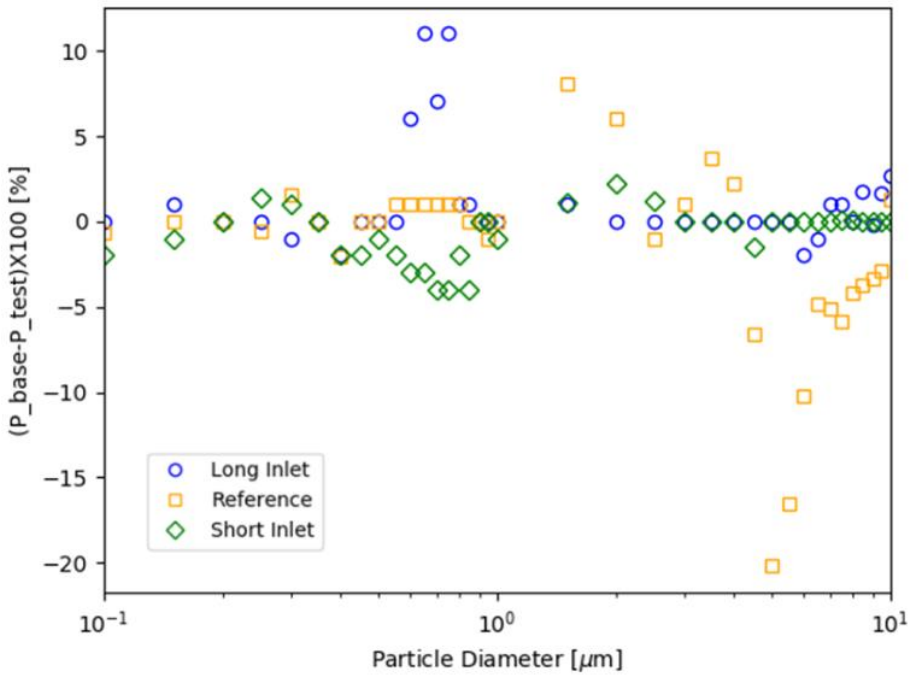

Figure 12. Full impactor mesh refinement study. The "Long Inlet," "Short Inlet," and "Reference" labels in the legend each correspond to a different impactor that was simulated. The base penetration is the penetration of the original mesh used, and the test penetration is the penetration of the 20% more fine mesh.

Finally, convergence for the full-impactor simulation is shown in Figure 13. From the figure, the simulation is well converged.

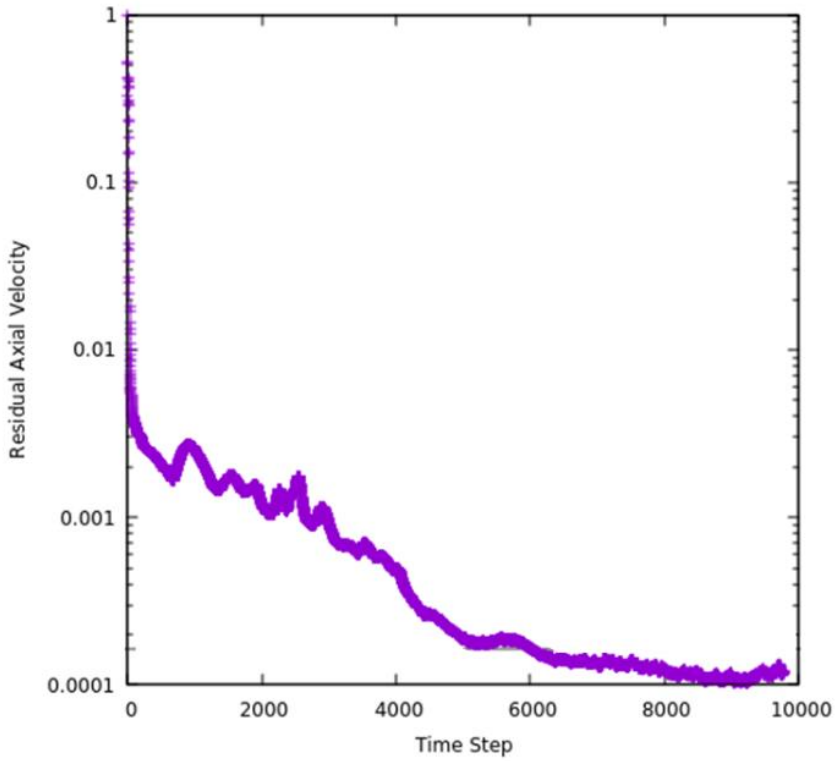

Figure 13. A plot of the axial velocity residuals versus simulation time step after taking on the previous result to demonstrate simulation convergence for the full impactor simulations

2.2 Experimental Methods

2.2.1 Impactor Design and Calibration

To validate the simulations, three single-stage nozzles were designed and tested. Two of the nozzle geometries were selected due to a combination of a high focusing score and good manufacturability. The third nozzle selected was a geometry which had previously been shown to demonstrate overfocusing, to serve as a reference. The critical geometry of all three impactors was the same, other than the three varied parameters described in section 2.1.1. The inlets to the nozzles were also different, such that the inlet length of each nozzle is seven times the diameter of the inlet. Figures 15-17 describe the geometries of the three nozzle designs. The Figure 15 geometry is referred to in subsequent sections as “Long Inlet,” Figure 16 is referred to as “Short Inlet”, and Figure 17 is referred to as “Reference.” The “Long Inlet” and “Short Inlet” geometries were selected from two simulated nozzle designs which were optimized for focusing. The “Reference” geometry is the same geometry as a previous study, which showed significant overfocusing at larger particle diameters (Eilts et al, 2021). This geometry was constructed to have a comparison for reference to help show that the nozzles optimized for focusing out-perform previously designed virtual impactor nozzles.

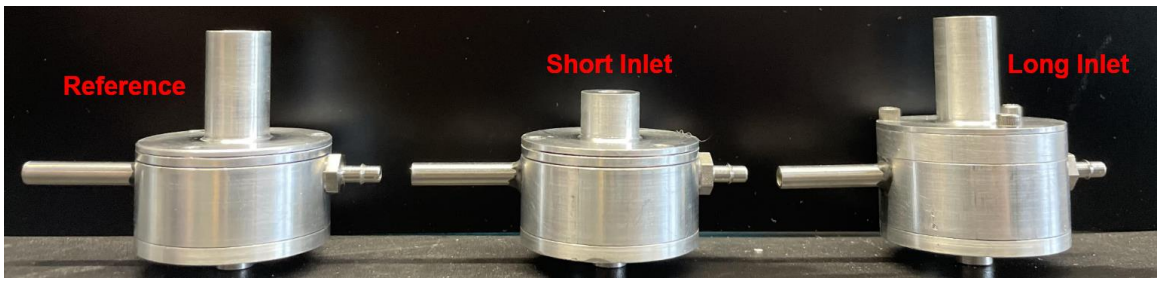

Figure 14. Image of all three manufactured impactors assembled.

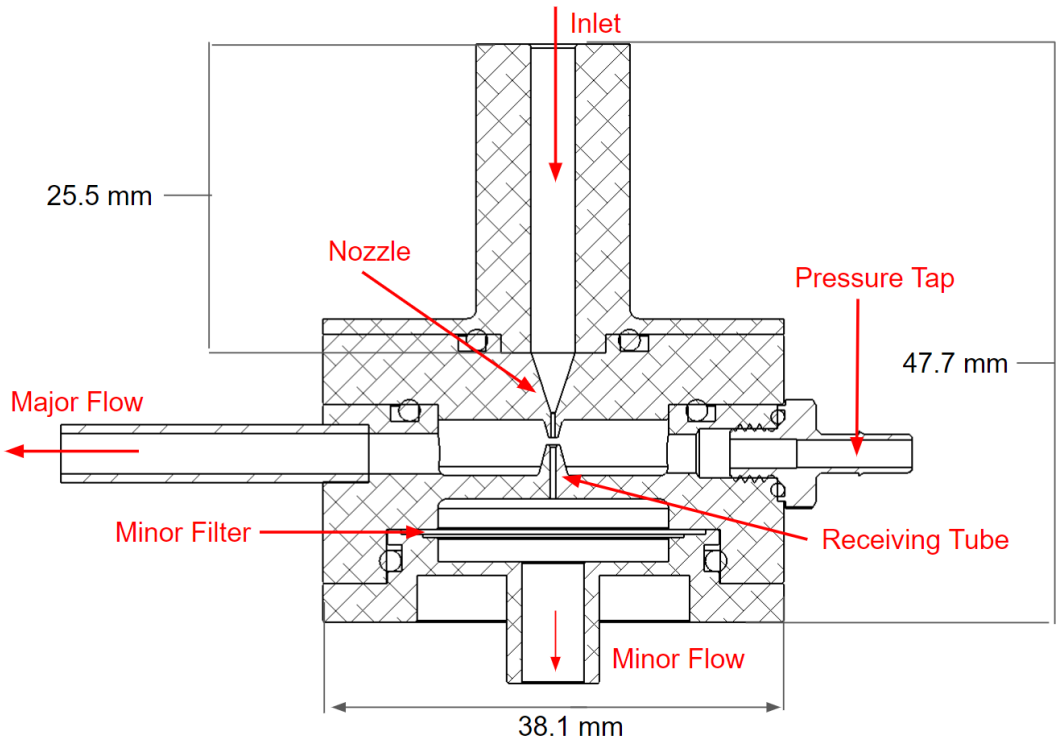

Figure 15. Cross-section of impactor from CAD model with key features of the impactor labeled. The geometry shown is optimized for focusing and referred to as the "Long Inlet" geometry due to the long nozzle inlet.

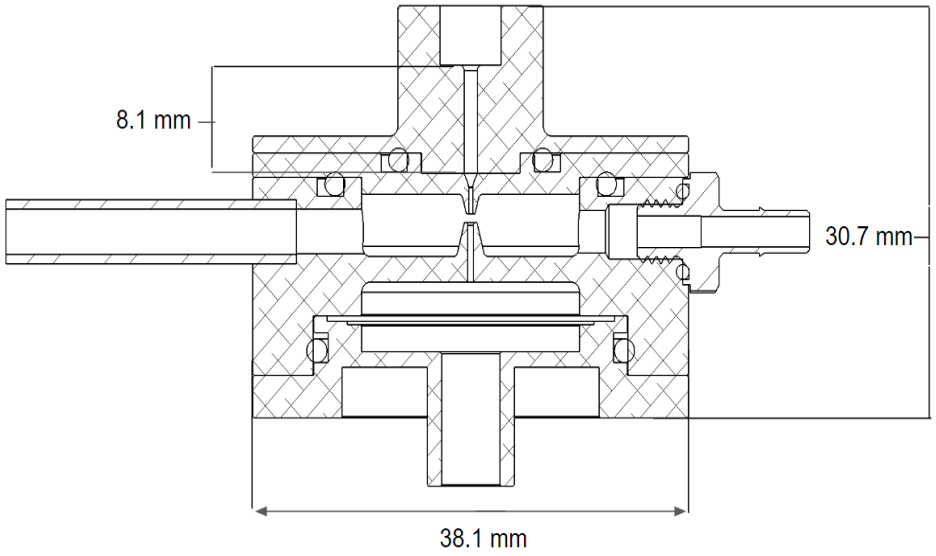

Figure 16. Cross-section of CAD model of the second impactor optimized for focusing. The geometry is referred to as the "Short Inlet" geometry due to its short nozzle inlet.

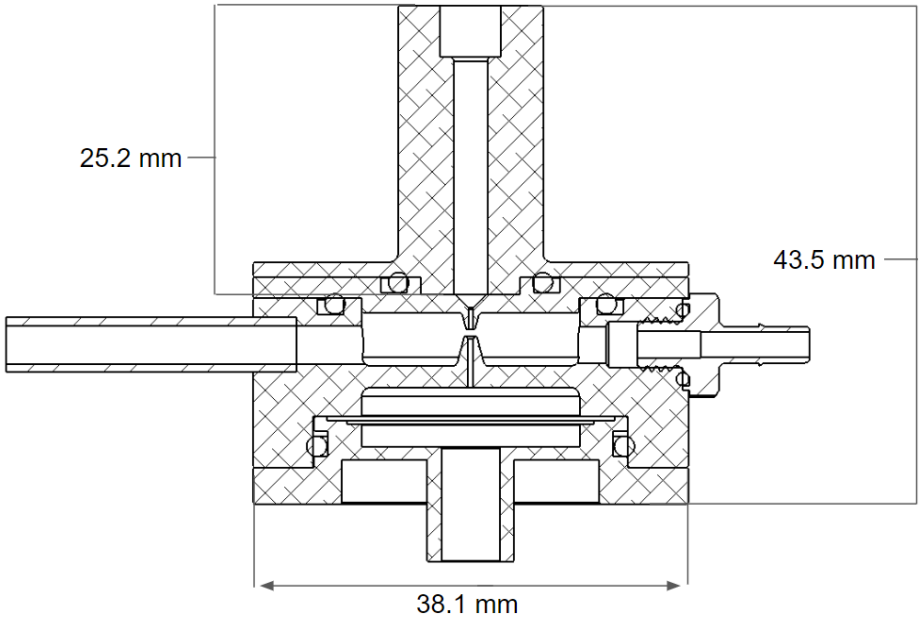

Figure 17. Cross-section of CAD model of the geometry which is not optimized for focusing. The geometry is referred to as "Reference" since its nozzle geometry was previously tested.

For all three impactors, the critical parameters which affect the nozzle Stokes number were held constant, including the nozzle diameter, the receiving tube diameter, and the nozzle to diameter distance. Therefore, all three impactors are nearly identical, other than the geometry of their inlets.

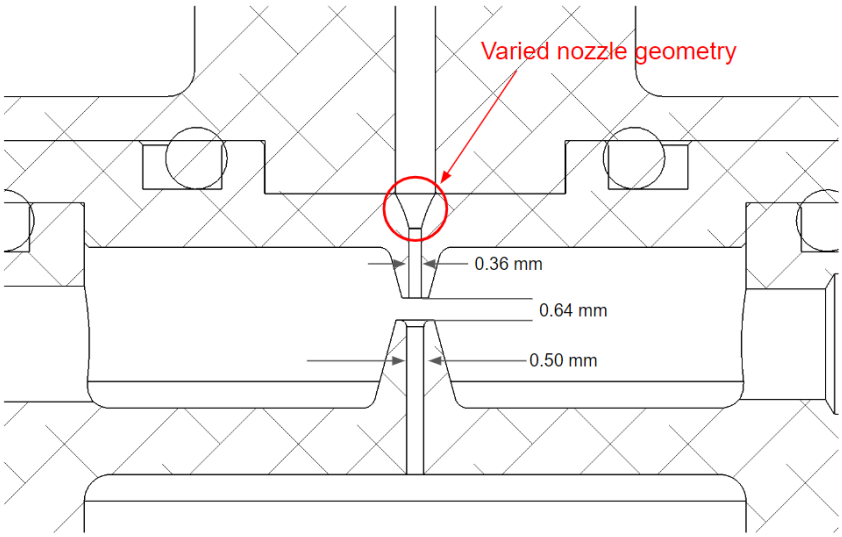

Figure 18. Figure depicting the geometry parameters which were held constant across all three impactors. The nozzle diameter, receiving tube diameter, and nozzle to receiving tube distance were all held constant.

All three impactors were calibrated by measuring the pressure in the major flow cavity as the total flowrate increased. All three impactors had similar calibration curves, reaching a flowrate of 1 LPM at approximately 65 kPa.

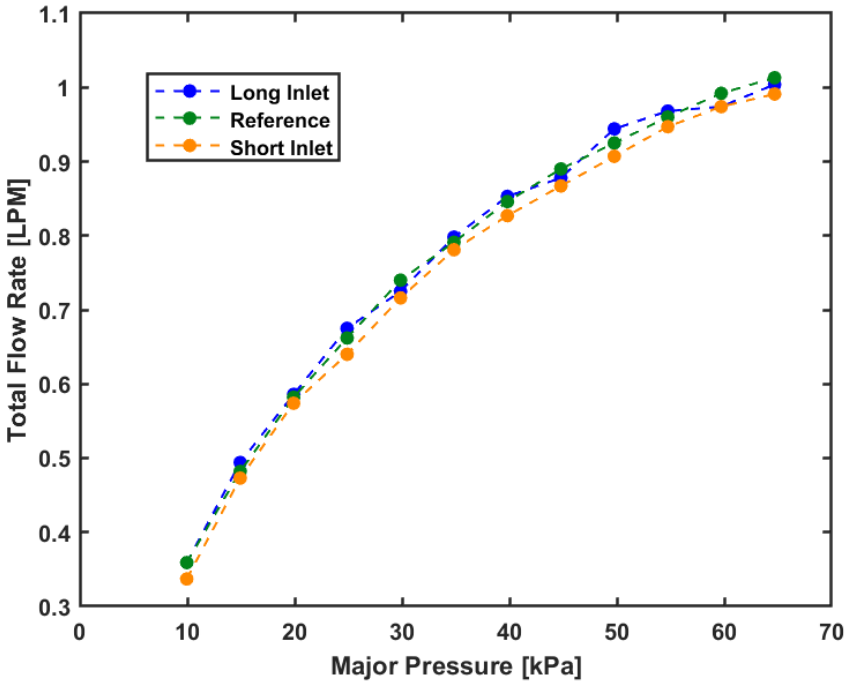

Figure 19. The total flow rate for each of the three impactors versus the pressure in the major flow cavity of the impactor

2.2.2 Atomizer with Polystyrene Latex Particles

PSL particles in the 0.5 μm to 3 μm diameter range were aerosolized using a constant output atomizer and used in virtual impactor calibration. A diagram of the experimental setup is shown in Figure 20. Fluorescent PSL particles of various diameters were run through the system until a sufficient signal was obtained. Filters placed at the outlets of the major and minor flows were used to collect the particles. The collection efficiency

and losses within the virtual impactor were then determined using fluoroscopy. All three impactors were tested at the same time. This ensured that testing conditions were consistent for each impactor. Calibrated pressure gauges were used to monitor the pressure in both the major and minor flows. Each component of the calibration system is described below.

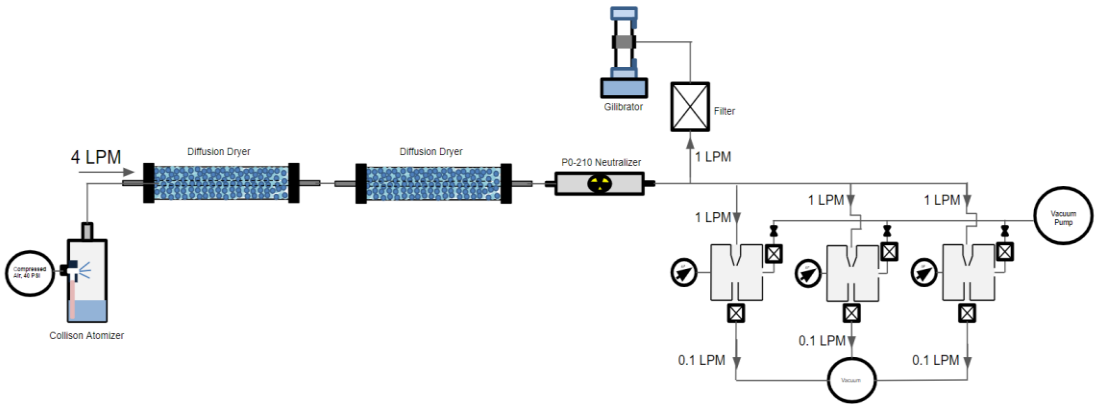

Figure 20. Diagram of experimental setup for fluorescent polystyrene latex particle testing. All three impactors were tested simultaneously.

Filtered, compressed air at 2.76 psi (19.0 kPa) was run through a pneumatic atomizer containing a suspension of fluorescent polystyrene latex (PSL, Magsphere) particles in 40 mL of deionized water. The particles were then run through two custom-made silica-bead diffusion driers to ensure that any water was removed. Finally, the particles entered a PO-210 neutralizer that ensured that they would have a net-neutral, near-steady state charge distribution. (Wiedensohler, 1988).

Before each test, the volumetric flow rate under standard conditions at the entrance to the impactors was recorded to ensure there were no leaks in the system and that the impactors were operated at the desired flow rate. The total flow through each impactor is 1 LPM (liter per minute) and is predetermined by its geometry, as the impactor operates close to its sonic limit at the nozzle throat provided the major flow pressure is sufficiently low and at the sonic limit the upstream volumetric flow rate is 1 LPM. 4 LPM was sent through the atomizer and diffusion driers, leaving an excess of 1 LPM to be measured. The minor flow for each impactor was controlled by a laminar flow element and vacuum pump and was set to be 0.1 LPM. All flows were monitored using a Sensidyne gilibrator.

Three tests were run at five PSL diameters (0.5 µm, 0.75 µm, 1.1 µm, 2.0 µm, 3 µm) for a total of 15 tests. Before each test, an Aerodynamic Particle Sizer (APS) was used to ensure that the particles were monodisperse and matched the expected PSL size selected. Each test was run for approximately twenty minutes. After a test ended, each virtual impactor was disassembled into its component parts and three regions within each impactor were swabbed for losses. Swabbing was performed by dipping a cotton swab into a beaker containing 10 mL of Methyl-ethyl Ketone (MEK), swabbing the impactor surface, then returning the cotton swab to the beaker. The major and minor filters were also each placed into beakers containing 10 mL of MEK. Beakers were then covered with Parafilm and the filters and swabs were left to soak for at least 20 minutes.

For the fluorometric analysis, 3 mL of the MEK-PSL suspension from each beaker were dispensed into test tubes. The tubes were then placed into a fluorometer, and the relative particle concentrations on each surface and filter were recorded.

2.2.3 Differential Mobility Analyzer with Fluorescent Polystyrene Latex Particles

For the testing of 50 nm and 200 nm particles, a differential mobility analyzer was required for the size-selection of particles. Without size-selection, the presence of surfactant can alter the size of the particle, leading to an incorrect result. The DMA (Differential Mobility Analyzer) tests were nearly identical to the fluorescent PSL particles described previously; differences were longer run-times and testing of one impactor at a time due to flowrate limitations. The DMA test run-time was approximately 45 minutes for the 200 nm test and 120 minutes for the 50 nm tests. A CPC (Condensation Particle Counter, Model 3776C) was used to check the size of particles to ensure the size-selection was accurate. A custom DMA was used (Knutson & Whitby, 1975).

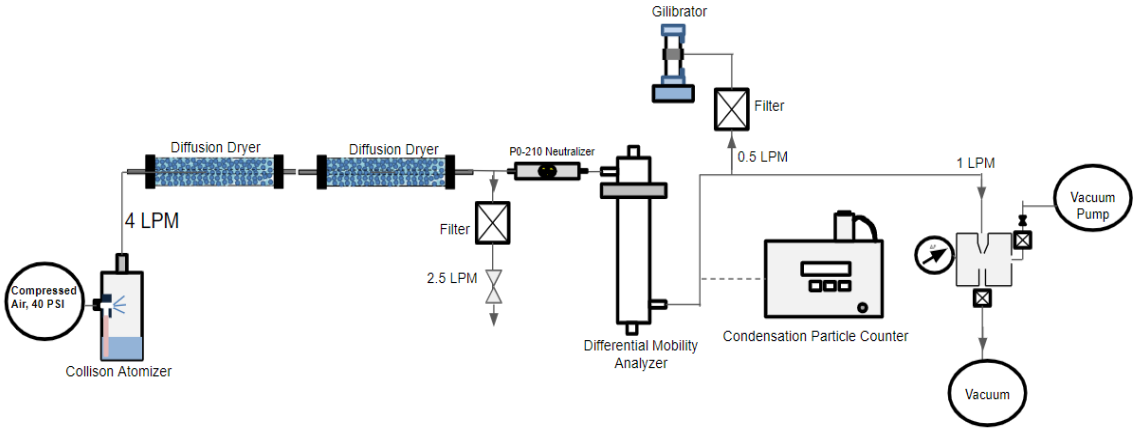

Figure 21. Diagram of experimental setup for testing using a differential mobility analyzer. Each impactor was tested individually.

2.2.4 Vibrating Orifice Aerosol Generator with Uranine Particles

For particles greater than 3 µm, a vibrating orifice aerosol generator (VOAG, TSI Model 3450) was used for calibration. The VOAG generated monodisperse droplets of oleic acid, which were tagged with uranine to make them fluorescent. The particle diameters generated with the VOAG were 4.3 µm and 6.5 µm. An APS was used to ensure that the particles were monodisperse. The total test duration was approximately 5 minutes. The swabbing and fluorometric analysis process was the same as for the PSL tests, except for the solvent used was 0.001 M NaOH. Figure 22 shows the experimental setup for the VOAG tests.

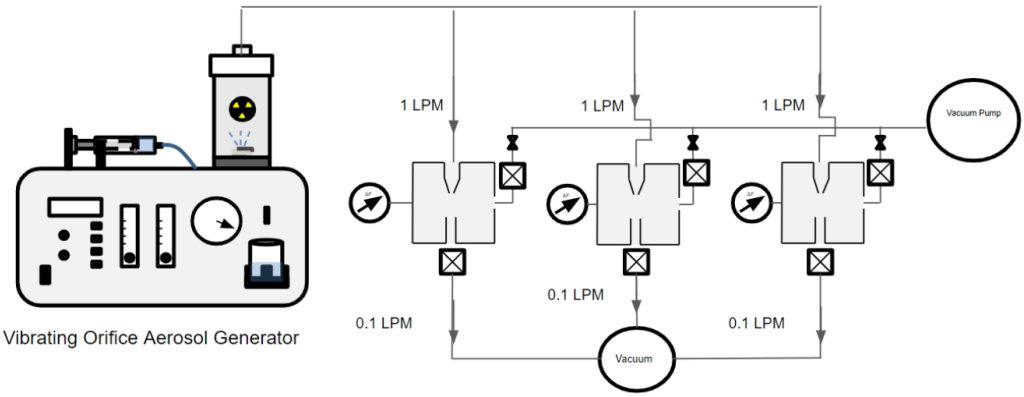

Figure 22. Experimental setup for testing using a vibrating orifice aerosol generator. All three impactors were tested simultaneously.

CHAPTER 3: RESULTS AND DISCUSSION

3.1 Overview

This section shows the results of simulation and experimental work on the study of inertial particle control for focusing. First, the CDF simulations and particle trajectory results from single-stage nozzles are presented, showing that the geometry of a nozzle has a significant impact on the trajectory of particles. The relationship between the geometry of a nozzle and its ability to focus particles is also explored via the scoring system established previously. Next, a similar study is performed for three different sets of two-stage nozzles, each with a set lower stage but varied upper stages. This result demonstrates the significance of the upper stage on the overall particle trajectories. Lastly, the experimental results from testing two virtual impactors with nozzles optimized for particle focusing are explored. These experimental results validate the simulated impactors, proving that it is possible to optimize the inertial control of particles via the modification of nozzle geometry.

3.2 Single-Stage Nozzles

The simplest case to be studied is that of a single-stage nozzle, with three varied design parameters: the inlet length, inlet radius, and radius of curvature. In this section, the CFD and particle trajectory results of single-stage nozzles are explored. Due to the large number of geometries analyzed, it is not possible to show all the results here. For a sense of the variety in geometries, the pressure, temperature, and velocity fields of a sample of 10 cases are in Figures 23-25.

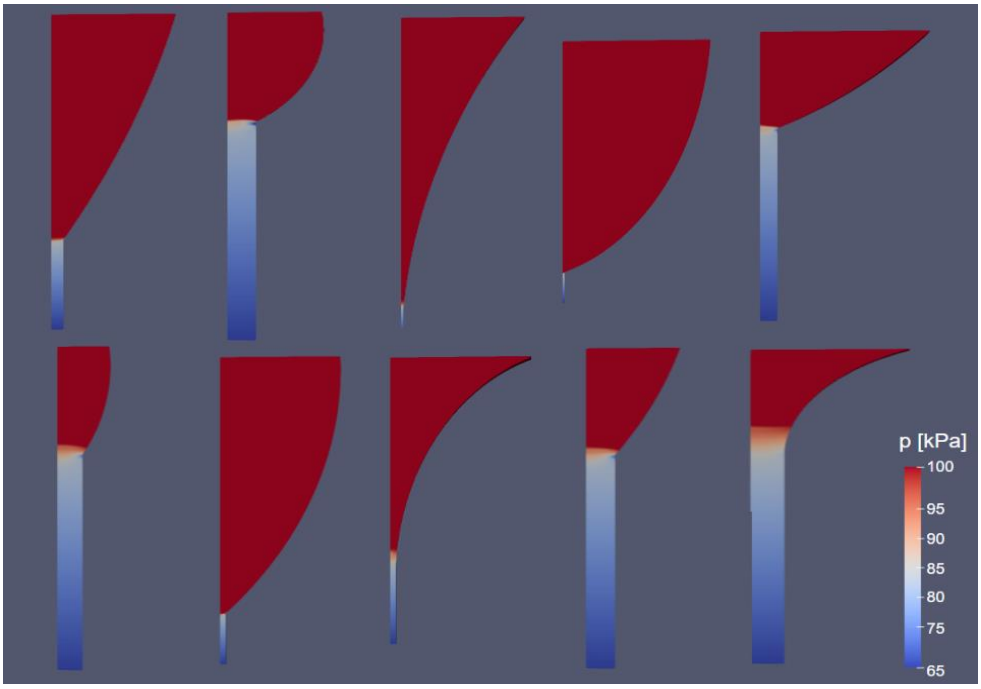

Figure 23. Sample pressure fields of ten different nozzles [kPa] with varied geometries

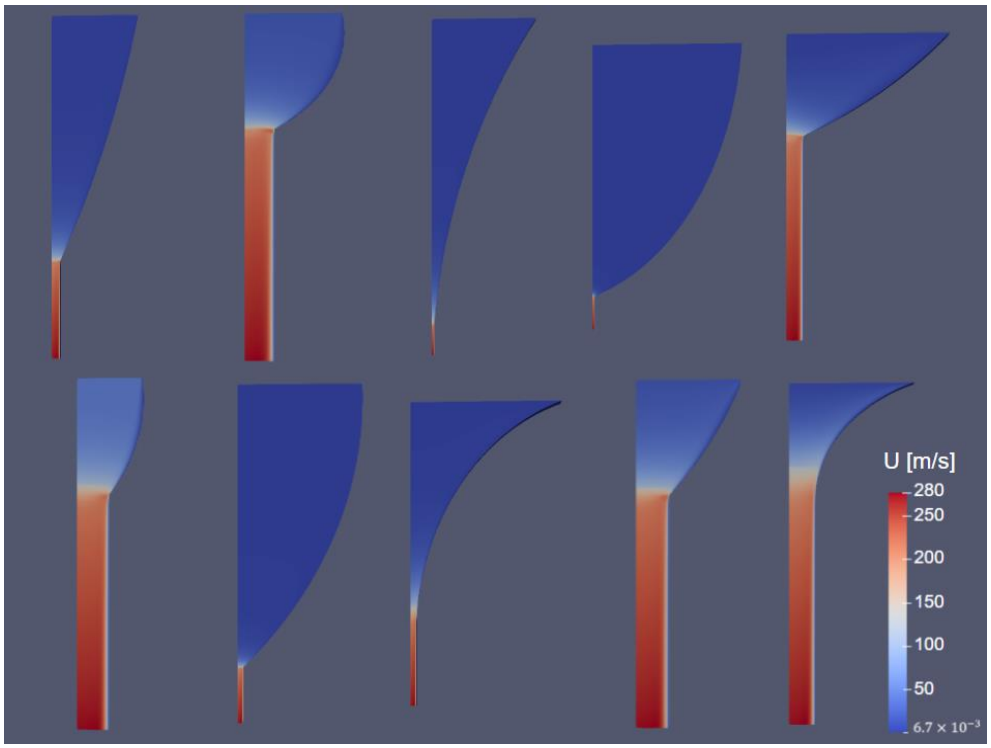

Figure 24. Sample velocity fields of ten different nozzles with varied geometries [m/s]

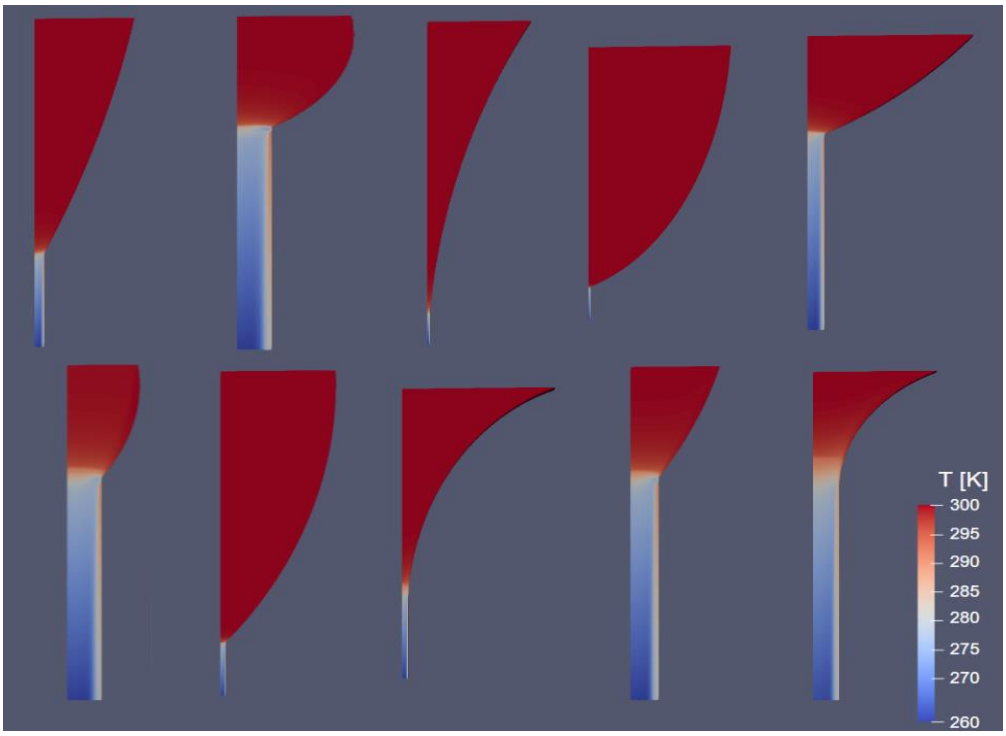

Figure 25. Sample Temperature fields of ten different nozzles with varied geometries [K]

Regarding velocity, all nozzles span similar ranges, with initial values low and dependent on the total inlet area, reaching up to a maximum velocity of approximately 280 m/s. The velocity does not quite reach supersonic speeds due to the low-pressure conditions set at the nozzle outlet. This condition is set to mimic the major flow pressure that will later be set when the nozzle is used in conjunction with a full virtual-impactor design. Although the ranges spanned across nozzles are similar, the overall development of the pressure, velocity, and temperature do vary across different geometries. These differences critically affect the trajectories of the particles through the geometries, leading to variations in the ability of each nozzle to effectively focus a wide range of particles to the centerline of the nozzle.

To understand how the ability of a nozzle to focus particles is affected by its geometry, the scoring system described previously was used to evaluate the effectiveness of each nozzle. As noted in the previous section, the score of a nozzle is the integration of the penetration of particles within a focused region of the nozzle exit (defined as 10% of its area) over the particle size range of interest.

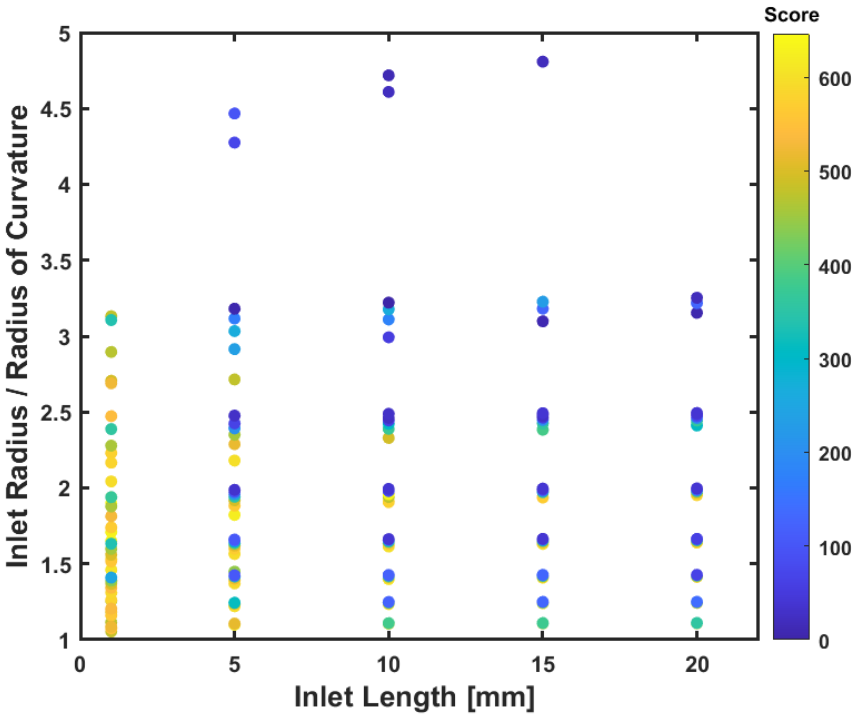

Figure 26. Scores of all nozzles simulated as a function of inlet length, inlet radius, and radius of curvature.

The score distribution of the nozzles is best understood by looking at the score as a function of the nozzle inlet length, as well as the ratio of inlet radius to radius of curvature, as seen in Figure 26. It was found that shorter nozzles generally had higher scores than longer nozzles. Scores were also better for smaller ratios of inlet radius to radius of curvature, with peak scores being observed around a ratio of two across all inlet lengths. A ratio of two is a straight inlet, meaning that this shape is consistently effective

independent of inlet length. A high inlet radius to radius of curvature ratio often indicated a more unusual geometry, with a large inlet radius as compared to the diameter of the nozzle entrance itself. Thus, it was found that the simplest geometries were often the most effective in focusing particles.

While the score of a nozzle is a good indication of how close particles are to the centerline of the nozzle at the nozzle exit, the trajectories must also be checked to see if overfocusing has already occurred. If particles are beginning to overfocus, despite having a good score, it is likely that they will be more overfocused at the entrance to the receiving tube of the virtual impactor, since they must continue their trajectories a small distance further after exiting the nozzle. To show the range of performance of the nozzles tested, Figures 27-29 display a variety of trajectories rather than the best trajectories achieved. The plotting of the trajectories leads to some distortion in the shape of the nozzle. Thus, an accurately scaled geometry is shown to the left of each trajectory plot for reference.

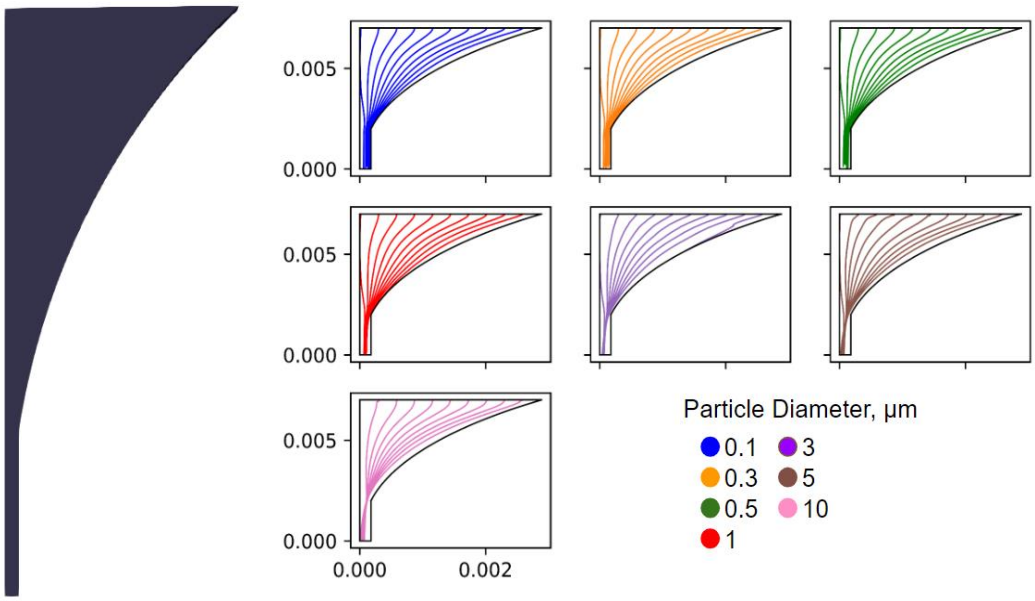

Figure 27. Sample trajectory for a geometry which has poor particle focusing. Particles are under focused, meaning that their final position upon exiting the nozzle is not close to the centerline of the nozzle.

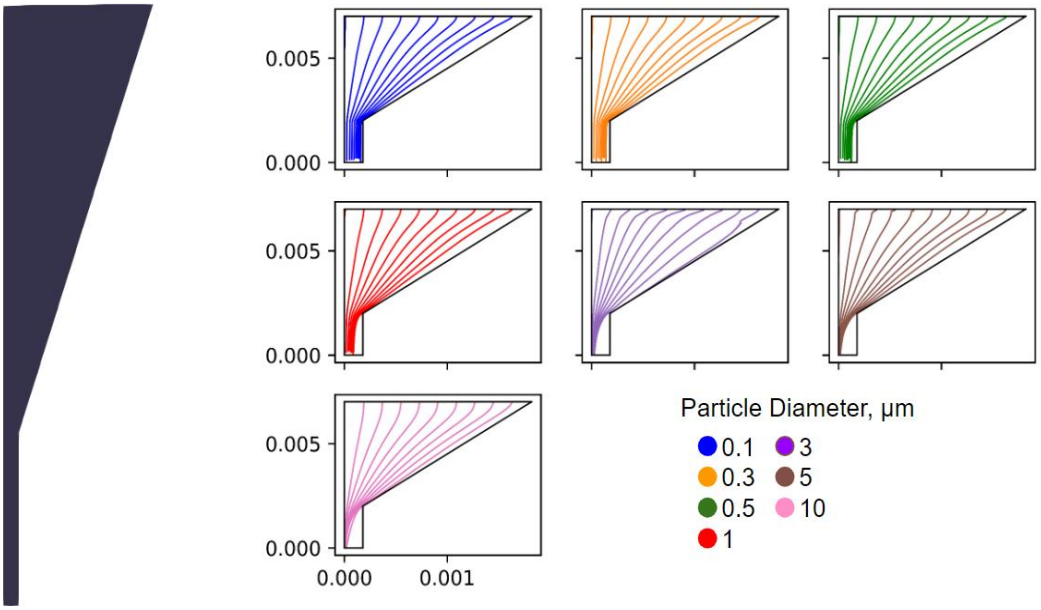

Figure 28. Sample trajectory demonstrating good focusing. Across all particle diameters, the final position of particles is close to the centerline of the nozzle at the time they exit the nozzle.

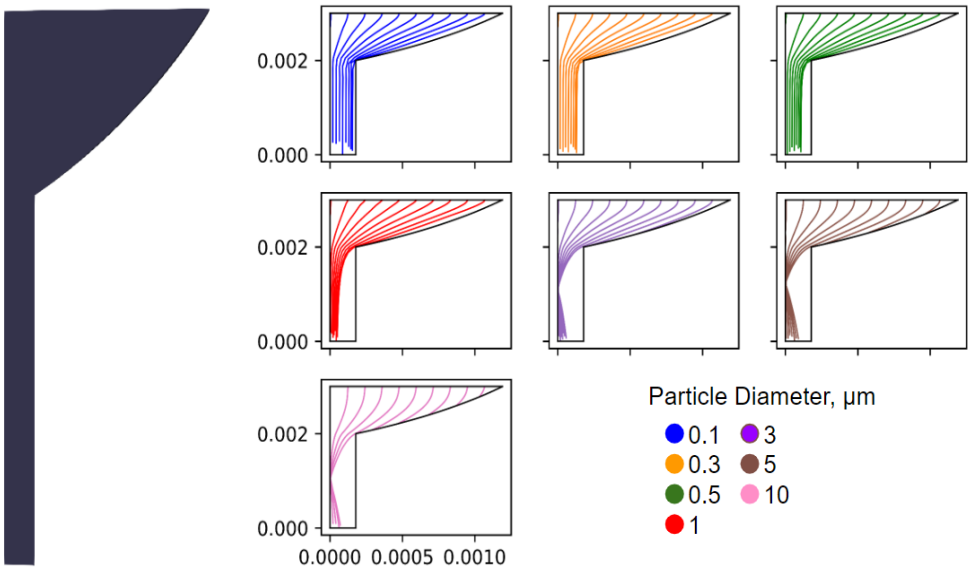

Figure 29. Sample trajectory demonstrating overfocusing. Particles reach a focused point about halfway through their trajectories, then their radial inertia carries them away from the centerline. At the nozzle exit, particles are spread out widely.

Figure 27 has a concave geometry and shows under-focusing. Even at smaller diameters, particles are shifted away from the centerline. Under-focusing was found to commonly occur in concave geometries, and thus these geometries are not ideal for focusing. Figure 28 has a straight geometry and shows near perfect focusing. This result further validates the trend shown previously that peaks in score tend to occur in nozzles with a ratio of inlet radius to radius of curvature of around two. Finally, Figure 29 shows the overfocusing phenomenon which we are seeking to avoid. Some trends are consistent across all nozzle geometries, one being that smaller particles are more difficult to focus since their low inertia makes it difficult to manipulate their trajectories. It is around 1 to 2

micrometers in diameter that the impact of the nozzle geometry becomes more apparent. Overall, the sample trajectories show that we can control the trajectory of particles solely via the modification of three geometry parameters.

3.3 Two-Stage Nozzles

While the trajectories of larger particles are relatively easy to control via the modification of nozzle geometry, the effect on smaller particles is not as easily achieved, since focusing smaller particles requires higher velocities which can de-focus larger particles. Thus, it may be desirable to consider the development of a two-stage nozzle, with a second stage (upper stage) which would focus the larger particles and a first stage (lower stage) which would focus the smaller particles. To do so, we assume independence between the two stages, as previously suggested by Vidal-de-Miguel & Fernandez de la Mora (2012).

In Figure 31, the trajectories of 3, 5, and 10 μm particles are shown for three different two-stage nozzle geometries. The lower stages of all three nozzles are identical and were selected based on the single-stage design which performed best based on its score in the 100 nm to 1 μm range. The trajectories of the same size particles for the corresponding single-stage nozzle are shown in Figure 30. The second stage is then modified with the goal of focusing particles within the 1 μm to 10 μm range. In Figure 31, the upper stage of all three nozzles are identical, other than their radius of curvature.

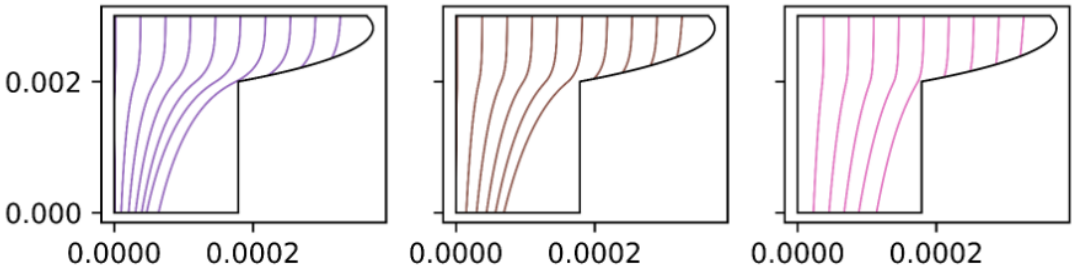

Figure 30. Trajectories of 3, 5, and 10 µm particles through a single stage nozzle.

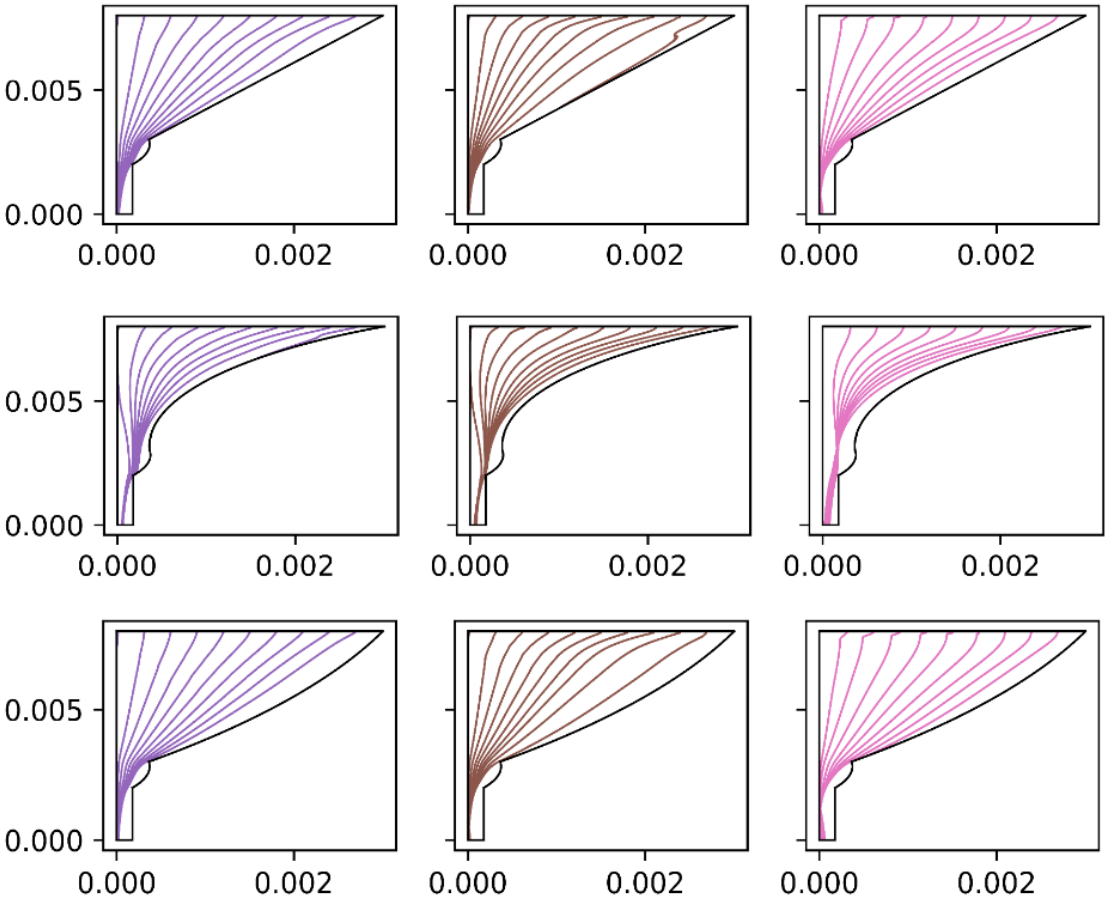

Figure 31. Trajectories of 3, 5, and 10 µm particles through three different two-stage nozzles. The lower stage of all three nozzles is identical to the geometry in Figure 30. The upper stages of all three nozzles are also the same, other than the radius of curvature.

Figures 30 and 31 show that the trajectory of particles is significantly impacted by the geometry of the upper stage. First comparing the single stage nozzle to the two-stage nozzles in Figure 31, we see that inlet losses are reduced for the first and third two-stage nozzles. Overall, however, there is no dramatic difference in focusing when comparing the single stage nozzle to the three two-stage nozzles. Next, considering the difference between the two-stage nozzles themselves, we see that even simply changing the concavity of the upper stage can switch the particle trajectory to be under focused or overfocused. The final position of particle is therefore highly dependent on the upper stage and the final position of the particle at the nozzle exit cannot be predicted by optimizing each stage separately for the focusing of different particle size ranges. Thus, the assumption that a focusing nozzle can be designed by considering a series of infinite contractions that are able to focus a range of sizes without defocusing any of the previous sizes is not correct.

To further understand why this assumption is not valid, the velocity profiles at the entrance to each stage of the nozzle must be considered. For single-stage nozzles, the flow at the entrance to the nozzle is uniform across the inlet. To add a second stage to the top of a previous nozzle without affecting the particle trajectories of the lower stage, a similar flow profile must be achieved. Otherwise, the simulation of the lower stage nozzle can no longer be validly used to select a geometry which can focus a range of particles independent of the upper stage.

Figure 32 shows the velocity profiles at a) the inlet of a single stage nozzle b) the velocity profile at the entrance to the same nozzle after adding a second stage to the top

of the nozzle, and c) the same combination of lower and upper stages, but with a straight section in between which is ten times the diameter of the inlet of the lower stage.

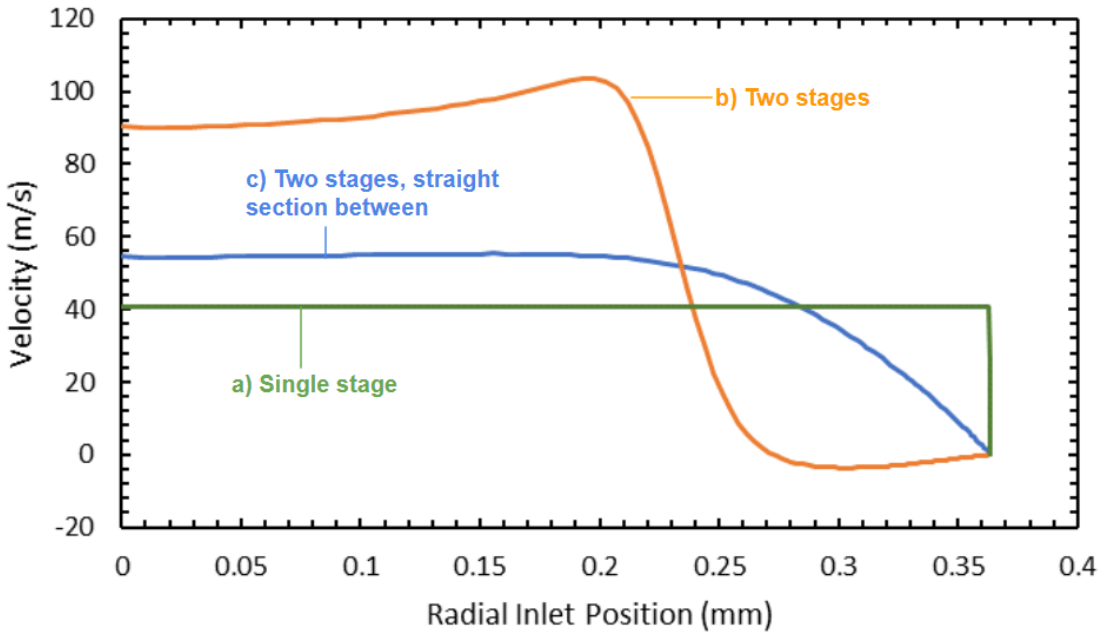

Figure 32. Velocity profile across the inlet of a single stage nozzle, a two-stage nozzle, and a two-stage nozzle with a straight section between the nozzles. The length of the straight section is ten times the diameter of the inlet of the lower stage.

Figure 32 shows that the addition of a second stage to a nozzle dramatically affects the velocity profile at the entrance to the nozzle. The overall magnitude of the velocity is significantly higher, with a peak about halfway across the radius of the nozzle before rapidly declining. This change in velocity profile tends to push smaller particles away from the center of the nozzle and results in two-stage nozzles which tend to improve focusing for larger particles but worsen focusing for smaller particles. To combat this problem, a potential solution is to add a long straight section between the two stages. This section allows for the flow to approach uniformity again and improves the

validity of the assumption that we can select each stage of the nozzle independently of each other. However, the profile does still differ, and further work must be done to investigate how effective the addition of this section is with regards to particle trajectory and focusing score.

Since it is not a valid strategy to first select a lower stage geometry that focuses smaller particles, then to next select an upper stage which focuses larger particles, it might be asked whether instead the opposite order should be considered: to first select the upper stage, and to then select the lower stage second. By doing so, the lower stage can then be varied while knowing the flow properties upstream, which will allow for accurate predictions of the final position of particles at the nozzle exit. However, in this case the problem remains complex. First, the possible geometries of the lower stage will be limited by the geometry of the upper stage since their inlet and outlet diameters must match at the junction between the stages. Either the outlet diameter of the upper stage must be allowed to vary, which adds additional complexity to the simulation, or the outlet diameter must be fixed, which limits the possible geometries for the lower stage.

Given the complexity of effectively selecting a two-stage nozzle, it must be asked whether a two-stage nozzle is in fact overall more effective than a single-stage nozzle. Figure 33 shows a sampling of 60 single-stage nozzle scores, placed in ascending order, as well as the scores of three sets of 60 two-stage nozzles. The two-stage nozzle sets each have a base corresponding to a single-stage nozzle with a high score in the 0.3 μm to 1 μm range, and the upper stage of the nozzle is varied. The two-stage nozzles are placed in line with the corresponding single stage case base geometry that it corresponds with. Note that the bases of the two-stage nozzles were selected based on high scores in the 0.3

μm to 1 μm range, which is why they do not match up with highest scoring single-stage nozzle cases, which are scored based on the overall performance from 0.3 μm to 10 μm.

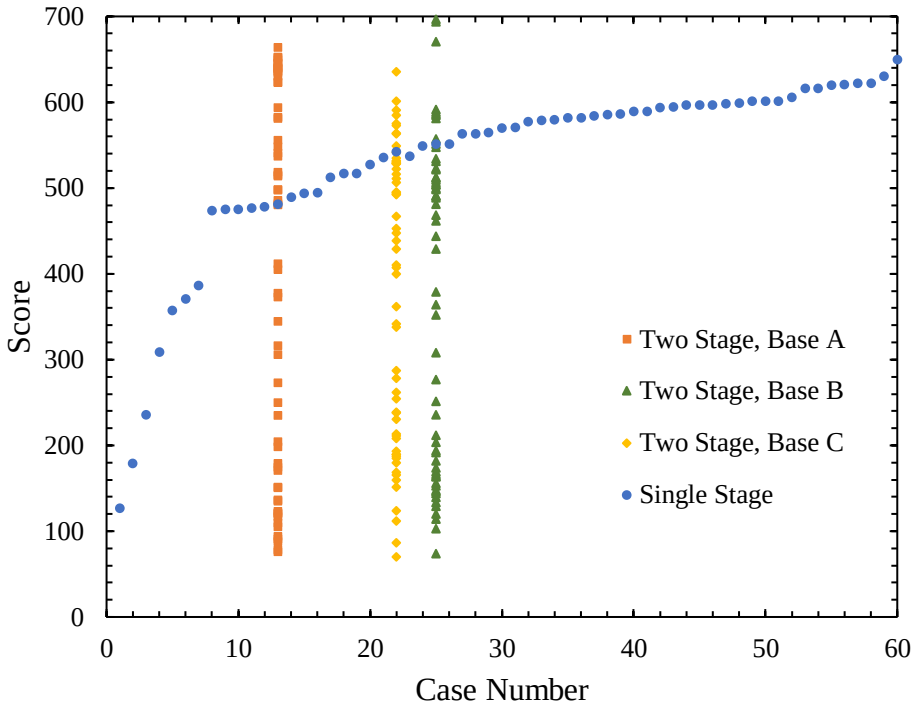

Figure 33. The score of a single stage nozzle for 60 different cases. Three sets of two stage nozzles are also plotted. The two stage nozzles each have a different set lower stage and varied upper stages. The scores of the two stage nozzles are plotted vertically in line with the single-stage case which their lower stage corresponds to.

From the figure, it is apparent that there are very few two-stage cases that outperform the best case from the single-stage nozzles. Additionally, we see that in most cases, the addition of a second stage to the nozzle worsens the overall performance, rather than improves it. The distribution of scores for the two-stage nozzles are similar,

suggesting that the performance of a two-stage nozzle is independent of the lower stage selected. This is further evidence that the two stages of the nozzle cannot be selected separately from one another. Although the two-stage nozzles explored here do not significantly outperform the single-stage nozzles tested, the conclusion is not that the addition of a second stage is not an effective method to improve focusing. Rather, two-stage nozzles must be further explored in the context of either complete randomization of both stages simultaneously, or the addition of a straight second between the stages which will help the flow velocity to reach a more uniform profile before the lower stage.

3.4 Virtual Impactor Experimental and Simulation Results

From the nozzle-only simulations, two of the highest scoring geometries were selected to be manufactured into virtual impactors and tested. These results were then compared to the results from testing a previous virtual impactor geometry, which was not optimized for focusing (Eilts et al 2021). The focusing optimized nozzles are referred to as “Long Inlet” and “Short Inlet,” while the reference impactor is referred to as “Reference.” To characterize the performance of a virtual impactor, the collection efficiency at all possible particle deposition locations must be determined. This consists of a total of five different locations: the inlet, major flow cavity, receiving tube, major filter, and minor filter. The goal of an impactor is to maximize the minor flow collection efficiency, while minimizing collection in all other regions, which are considered losses.

The minor flow collection efficiency determines the ability of an impactor to concentrate particles, and as such is the characterizing curve which defines the impactor’s performance. The collection efficiency is low at small particle diameters, and then begins to increase dramatically around the cut-point, which for all three of these impactors was

0.3 µm. Theoretically, the collection efficiency should approach 100% past the cutpoint. However, the collection efficiency often begins to decrease again due to overfocusing of large particles. Figure 34 and Figure 35 show the minor flow collection efficiencies for all three impactors as a function of particle diameter as well as Stokes number. Simulated points are represented as empty shapes connected by a dashed line. Experimental points are represented by solid shapes.

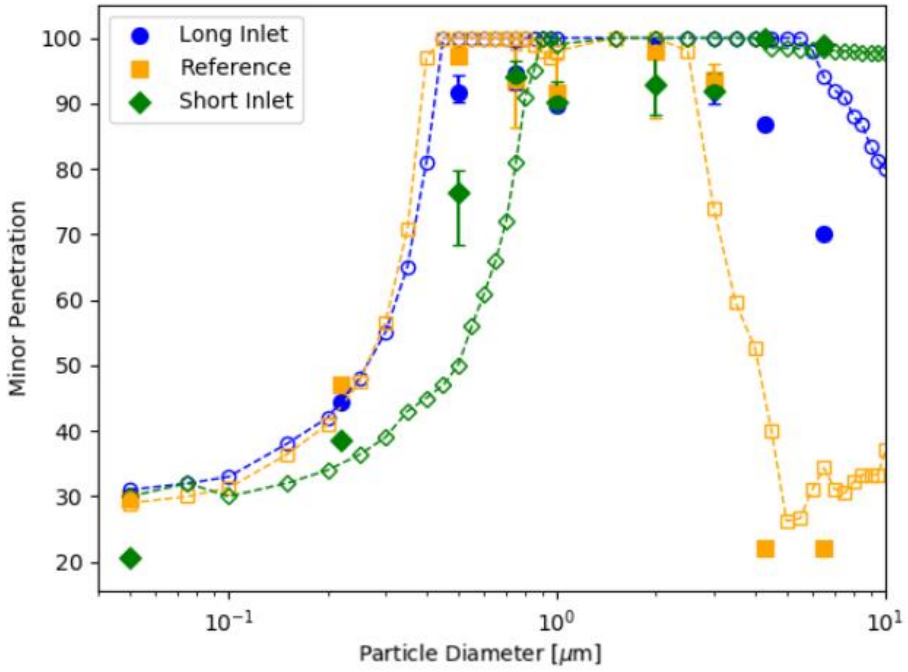

Figure 34. Penetration of particles into the minor flow versus particle diameter for the three different impactor geometries. Experimental points are represented by solid shapes, and simulated points are represented as empty shapes connected by a dashed line.

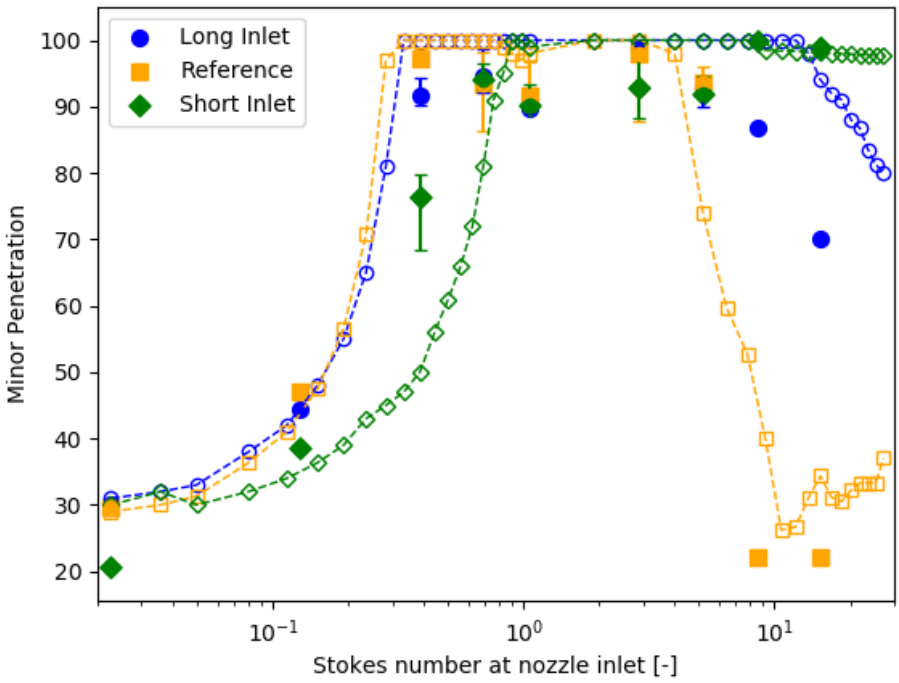

Figure 35. Penetration of particles into the minor flow versus Stokes number for the three different impactor geometries. Experimental points are represented by solid shapes, and simulated points are represented as empty shapes connected by a dashed line.

To begin, we see that the experimental data points for all three tested impactors match well with their simulated curves. Therefore, the simulated points can be considered accurate predictors for the performance of the impactors, which will be useful for the further development of virtual impactors optimized for focusing. Comparing the three different impactors, the "Short inlet" geometry shows worse penetration at smaller particle diameters, but much improved penetration at larger particle diameters. In fact, at the larger particle diameters there is no evidence of overfocusing, and penetration remains high. For the "Long inlet" case, the penetration at small particle diameters is very

similar to that of the “Reference” case. However, at larger particle diameters the penetration is once again significantly improved from the “Reference” case. Overall, the reduction in overfocusing is approximately 80% for the “Short inlet” case, and 60% for the “Long inlet” case.

Regarding Stokes number, the “Long inlet” and “Reference” cases have a critical Stokes number of approximately 0.15 both experimentally and from the simulation, while the “Short inlet” case has a critical Stokes number of approximately 0.4 from the simulation, and a slightly lower Stokes number experimentally. This translates to a critical particle diameter of 0.25 μm for cases “Long inlet” and “Reference,” and 0.5 μm for the “Short inlet” case. For comparison, the impactors were all designed to have a cutpoint of 0.3 μm. This suggests that the geometry of the nozzle inlet can affect Stokes number, despite not being a variable in its definition. In fact, the classic definition of Stokes number used for impactor design is not well-suited to compressible, high Reynold’s number flow. This is because the classic definition of Stokes number assumes a linear relationship between drag and relative particle velocity, which is not true at high Reynolds numbers (Eilts et al 2021).

Another method of comparing the performance of the impactors is to look at receiving tube losses. When overfocusing occurs, it most often leads to deposition within the receiving tube of the impactor. Therefore, a reduction in receiving tube losses is an indicator of improved particle focusing. Figure 36 shows the receiving tube collection efficiency for the "Long inlet," "Short inlet" and "Reference" geometries.

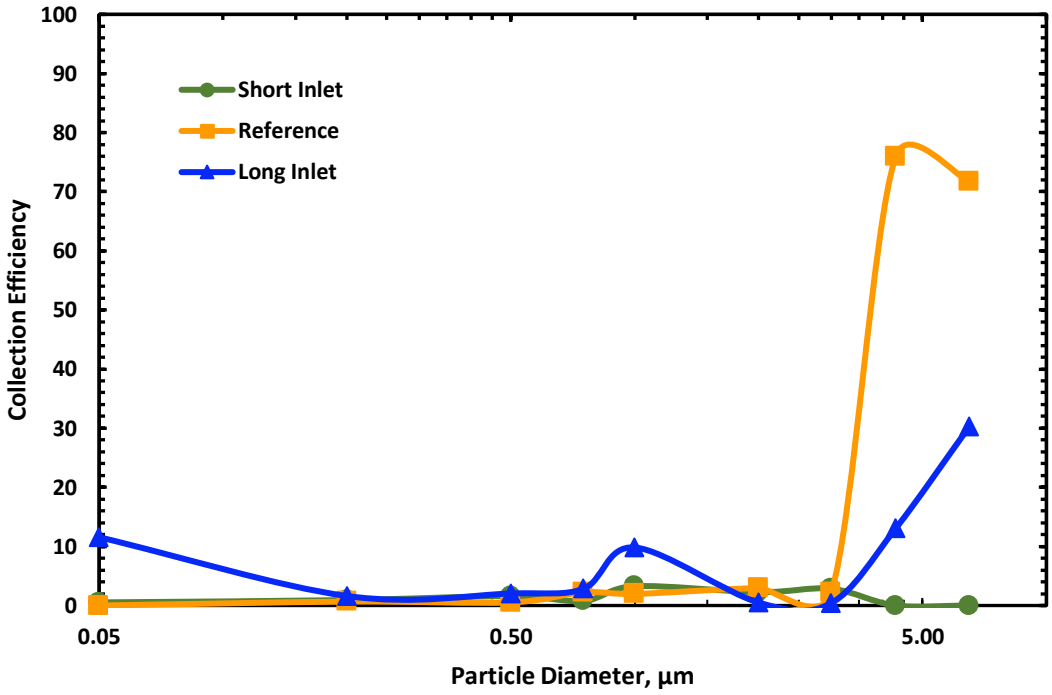

Figure 36. Receiving tube collection efficiency versus particle diameter plotted for each of the three impactors tested.

Figure 36 shows a significant reduction in receiving tube losses in the cases which are optimized for focusing. The maximum receiving tube collection efficiency for the reference case is 75.9%, while the maximums for the "Long inlet" and "Short inlet" cases

are 30.3% and 5.8%, respectively. The reduced receiving tube losses prove that the optimized cases effectively improve the ability of the impactor to focus particles.

For the final evidence of the improved focusing capability of the optimized nozzles, we can look at visual evidence of focusing occurring on the minor flow filter. Figure 37 shows 4.3 µm particles stacking into a very tall and thin column onto the minor flow filter of the "Short inlet" geometry. This particle stacking shows that not only are particles sufficiently focused such that receiving tube losses are minimized, but that their final trajectories are close enough to the centerline that they are able to deposit into a small beam. This deposition pattern demonstrates not only excellent focusing, but also consistency, since the final location of particles does not vary with time or slight variations in conditions within the impactor.

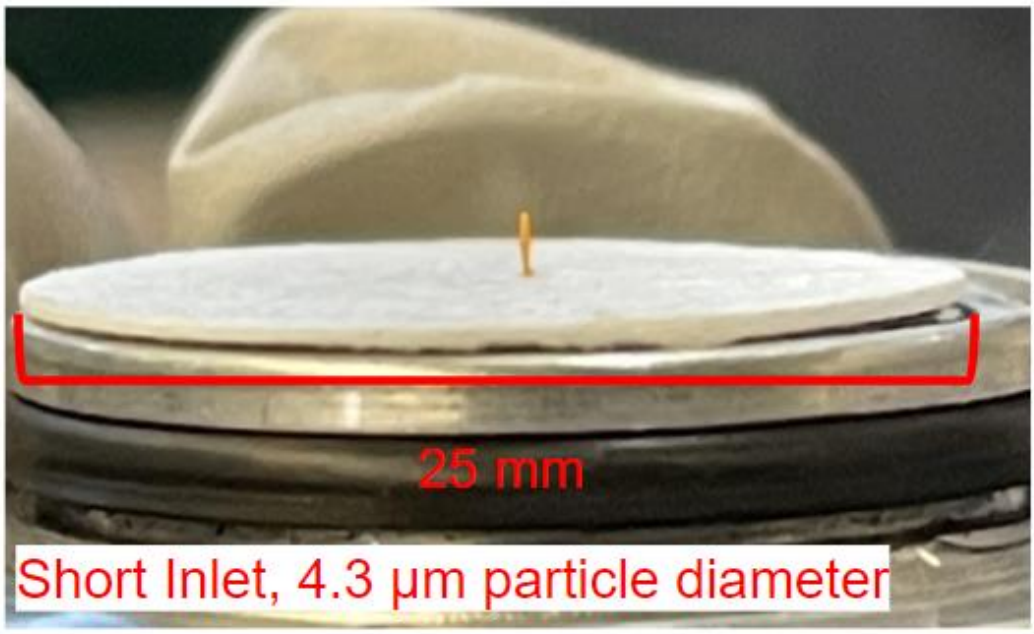

Figure 37. Visualization of 4.3 µm particle focusing onto the minor flow filter of the "Short Inlet" geometry.

CHAPTER 4: CONCLUSIONS

The goal of this study was to design a nozzle optimized for particle focusing, and then use this nozzle in a virtual impactor to decrease particle losses and improve the concentration factor of the virtual impactor over a wide range of particle diameters. Two virtual impactors were constructed with nozzles optimized for focusing, which led to a significant improvement in the particle concentration factor, particularly at particle diameters in the 2-10 μm range, where overfocusing typically occurs. Therefore, the study shows that the modification of nozzle inlet geometry can significantly affect the performance of a virtual impactor.

The results of this study are of interest both specifically to virtual impactor research, as well as more generally to any application in which the focusing of particles is desired. Regarding virtual impactors, one growing research area is the concentration of submicrometer particles for sampling of SARS-CoV-2. It is difficult to sample viruses, as they are potentially transported in submicrometer particles and exist in low concentration in the air. Obtaining a sufficient sample requires running a sampler for an extended period, which is not typically done (Fabian, McDevitt, Houseman, & Milton, 2009). Furthermore, samplers do not often separate particles by size and are inefficient at sampling submicrometer particles. An additional complication of viral sampling is that the viruses must remain active and undamaged during the sampling process (Fennelly, Tribby, Wu, Heil, Radonovich, Loeb, & Lednicky, 2015). Virtual impactors address many of the key issues associated with viral sampling, as they can sufficiently

concentrate submicron particles into detectable quantities yet remain gentle enough with the particles to retain their cellular viability (Ho, 2011).

Another application for virtual impactors is particle concentration for indoor or outdoor air quality sampling. For air quality research, it is often desired to sample particles less than 2.5 µm, as elevated concentrations of these particles have been shown to have negative health effects, such as respiratory illness and cardiovascular problems. (Singer & Delp, 2018). Sensors which detect particles via light scatter have become popular for air quality monitoring, however, their capabilities are strongly dependent on the particle size distribution. Furthermore, for outdoor air sampling, these devices are also sensitive to environmental factors. In comparison, virtual impactors have high separation efficiency and relatively low losses, and the 2.5 µm cutpoint often desired for air sampling is easily achieved (Li & Yanna, 2021). For any type of virtual impactor sampling application, whether SARS-CoV-2 or air quality monitoring, it is desirous to maximize the minor flow collection efficiency. Therefore, the optimized impactors designed in this study would be useful to many applications of virtual impactors.

In addition to use in a virtual impactor, particle focusing can also be more generally applied to other situations in which it is desirous to concentrate or focus particles. For example, the same optimized nozzle geometries could be used for other concentrating devices, such as cascade impactors, traditional impactors, or even high volume concentrators. In all of these applications, it is desirous to minimize losses, and improve the ability of the system to concentrate particles. Therefore, an optimized nozzle could be translated to a variety of sampling and concentration applications. Finally, particle focusing could be useful for 3D printing, in which it would be advantageous to be able to

pack a printer with a wide range of particle sizes and focus them all into a small beam along the nozzle centerline, resulting in a very fine print.

This study shows that the performance of a virtual impactor can be dramatically altered solely via modification of the geometry of the nozzle inlet. There are several extensions of this work that would be interesting to explore. First, it would be useful to define a new Stokes number, which accounts for the changes in particle behavior due to flow compressibility. Israel and Rosner (1982) have proposed a modified Stokes number which depends on Reynolds number and Mach number, which could be useful for more accurate impactor design. This method would require integration of conditions across the nozzle geometry, and hence would necessitate an iterative approach for design.

Another potential extension would be to re-design the same impactor(s) analyzed in this study, but with a reduced receiving tube size. Since the impactors are optimized for focusing, the trajectories of particles are closer to the centerline of the receiving tube than non-optimized impactors. Thus, the need to widen the receiving tube in order to reduce particle losses is not as important, and its size can be reduced. Studies have shown that a reduction in the ratio of receiving tube to nozzle diameter helps to decrease the overall losses within an impactor, as well as shift the cutpoint lower (Sioutas, Koutrakis, & Olson, 1994). Therefore, a focusing nozzle can help to obtain a smaller cutpoint, which is often desirable for the sampling of viruses.

Another continuation of this work would be the further development of two-stage nozzles. In this study, it was shown that the stages of two stage nozzles cannot be selected independently of one another. It was also shown that the addition of a straight section between the two stages of the nozzle can help the stages to become increasingly

independent. The effect this addition has on the score was not investigated, and it would be interesting to see to what degree a straight section could increase the validity of selecting the stages independently. Otherwise, if it is not desirous to add a straight section between the stages, it would also be good to attempt to improve focusing via simultaneously changing both stages of the nozzle.

For the development of focusing nozzles specific to virtual impactors, it would be useful to extend the same study of varying nozzle geometries to be performed within a full virtual impactor. While it was shown that the scoring system for nozzle only simulations effectively predicted nozzles which would show improved focusing performance, the exact penetration curve of the full impactor cannot be predicted from the nozzle only simulations. Thus, it would be useful to explore how the modification of nozzle geometry could shift the penetration curve to focus on a particular size range of interest. For example, the “Short inlet” case performed extremely well at larger particle diameters, but not as well for smaller particle diameters. It would be a useful tool when designing impactors if the penetration curve could easily be predicted and optimized for a desired size range of interest.

Regarding the prediction of nozzle performance, it would also be interesting to predict the focusing performance of a nozzle as a function of the nozzle geometry and flow parameters. This could be done in the form of a theoretical expression, which would be able to predict the location at which particle focusing will be optimized. Another potential solution would be to program parameters into a neural network, which would be able to predict the focusing score of a nozzle based on the desired inputs. This would aid in the design of impactors, allowing impactors to be rapidly designed for the desired flow

rate, cut point, etc. This study showed that nozzles can be successfully optimized for focusing, therefore improving particle concentration within a virtual impactor, and opening up new possibilities for the optimized performance of aerosol devices.

REFERENCES

C. Sioutas , P. Koutrakis & B. A. Olson (1994) Development and Evaluation of a Low Cutpoint Virtual Impactor, Aerosol Science and Technology, 21:3, 223-235, DOI: 10.1080/02786829408959711

Eichler, T., de Juan, L., and Fernandez de la Mora, J. (1998). Improvement of ´ the Resolution of TSI's 3071 DMA via Redesigned Sheath Air and Aerosol Inlets. Aerosol. Sci. Technol., 29(1):39–49.

E.O. Knutson, K.T. Whitby, Aerosol classification by electric mobility: apparatus, theory, and applications, Journal of Aerosol Science, Volume 6, Issue 6,1975, Pages 443-451, ISSN 0021-8502, https://doi.org/10.1016/0021-8502(75)90060-9.

Fabian, P., McDevitt, J. J., Houseman, E. A., & Milton, D. K. (2009). Airborne influenza virus detection with four aerosol samplers using molecular and infectivity assays: considerations for a new infectious virus aerosol sampler. Indoor air, 19(5), 433–441. https://doi.org/10.1111/j.1600- 0668.2009.00609.x

Fennelly K, Tribby M, Wu C, Heil GL, Radonovich L, Loeb J, Lednicky JA. Collection and measurement of aerosols of viable influenza virus in liquid media in an Andersen cascade impactor. Virus Adaptation and Treatment. 2015;7:1-9 https://doi.org/10.2147/VAAT.S7478

Fuerstenau, S., Gomez, A., and Fernandez de la Mora, J. (1994). Visualization of Aerodynamically Focused Aerosol Jets. J. Aerosol Sci., 25:165–173

Gatski, T. B. and Bonnet, J.-P., "Compressibility, Turbulence and High Speed Flow," 2009, Elsevier, Amsterdam

Guillermo Vidal-de-Miguel & Juan Fernandez de la Mora (2012) Continuously Converging Multistage Focusing Lenses to Concentrate Aerosols at High Reynolds Numbers, Aerosol Science and Technology, 46:3, 287-296, DOI: 10.1080/02786826.2011.621906

He J, Novosselov IV. Design and Evaluation of an Aerodynamic Focusing Micro-Well Aerosol Collector. Aerosol Sci Technol. 2017;51(9):1016-1026. doi: 10.1080/02786826.2017.1329515. Epub 2017 May 24. PMID: 30739977; PMCID: PMC6368264.

Hinds, W. (1999). Properties, Behavior, and Measurement of Airborne Particles (2nd ed.). Wiley-Interscience.

Ho, J. (2011). Use of Virtual Impactor (VI) Technology in Biological Aerosol Detection. KONA Powder and Particle Journal, 29, 16–26. https://doi.org/10.14356/kona.2011006

Israel, R., & Rosner, D. E. (1982). Use of a generalized stokes number to determine the aerodynamic capture efficiency of non-stokesian particles from a compressible gas flow. Aerosol Science and Technology, 2(1), 45–51. https://doi.org/10.1080/02786828308958612

Li, Yanna, et al. "A Combined Virtual Impactor and Field-Effect Transistor Microsystem for Particulate Matter Separation and Detection." Nanotechnology and Precision Engineering, vol. 4, no. 1, 1 Mar. 2021, p. 013003, https://doi.org/10.1063/10.0003447. Accessed 7 Mar. 2023.

Lin, H., & Heintzenberg, J. (1995). A theoretical study of the counterflow virtual impactor. Journal of Aerosol Science, 26(6), 903–914. https://doi.org/10.1016/0021-8502(95)00024-7

Liqiang Qi, Mengmeng Liu, Xu Wang, Jingxin Li, and Fang Zeng. Inertial Separation of Particles Escaped from Electrostatic Precipitators. ACS Omega 2021 6 (16), 10875-10883. DOI: 10.1021/acsomega.1c00624

Mahdavipour, O, Fahimi, D., Paprotny, I. Focusing of airborne particles using groove-induced envelope (GRIP) flow air-microfluidic concentrator. Journal of Microelectromechanical Systems, 2019

Mahdavipour, O., Fahimi, D., Paprotny, I. "Microfabricated Air-Microfluidics Virtual Impactor with Groove-Based Envelope-Flow Particle Focusing System," 2019 20th International Conference on Solid-State Sensors, Actuators and Microsystems & Eurosensors XXXIII (TRANSDUCERS & EUROSENSORS XXXIII), 2019, pp. 805-808, doi: 10.1109/TRANSDUCERS.2019.8808503.

Marple VA, Chien CM. Virtual impactors: a theoretical study. Environ Sci Technol. 1980 Aug 1;14(8):976-85. doi: 10.1021/es60168a019. PMID: 22296546.

Nils Roth, Salah Awel, Daniel A. Horke, Jochen Küpper,Optimizing aerodynamic lenses for single-particle imaging, Journal of Aerosol Science,Volume 124,2018,Pages 17-29,ISSN 0021-8502,
https://doi.org/10.1016/j.jaerosci.2018.06.010.

S.V Patankar, D.B Spalding, A calculation procedure for heat, mass, and momentum transfer in three-dimensional parabolic flows. International Journal of Heat and Mass Transfer, Volume 15, Issue 10,1972, Pages 1787-1806,ISSN 0017-9310, https://doi.org/10.1016/0017-9310(72)90054-3.

Schreiner J, Voigt C, Mauersberger K, McMurry P, Ziemann P (1998). Aerodynamic lens system for producing particle beams at stratospheric pressures. Aerosol Science and Technology, 29(1), 50–56.

Singer, BC, Delp, WW. Response of consumer and research grade indoor air quality monitors to residential sources of fine particles. Indoor Air. 2018; 28: 624–639. https://doi.org/10.1111/ina.12463

Stephanie M. Eilts, Tomoya Tamadate, Mckenna E. Relling, Ian A. Marabella, Christopher J. Hogan, Bernard A. Olson, Virtual impaction in compressible flows with pressure recovery, Journal of Aerosol Science, Volume 167, 2023, 106076, ISSN 0021-8502, https://doi.org/10.1016/j.jaerosci.2022.106076.

Virgil A. Marple (2004) History of Impactors—The First 110 Years, Aerosol Science and Technology, 38:3, 247-292, DOI: 10.1080/02786820490424347

Woo, J. L., Sareen, N., Schwier, A. N., and McNeill, V. F.: Concept for an electrostatic focusing device for continuous ambient pressure aerosol concentration, Atmos. Meas. Tech., 12, 3395–3402, https://doi.org/10.5194/amt-12-3395-2019, 2019.

Ying, Y., Lin, Y. Inertial Focusing and Separation of Particles in Similar Curved Channels. Sci Rep **9**, 16575 (2019). https://doi.org/10.1038/s41598-019-52983-z

Appendix- Figure Permission

Figure 3 Permission:

Optimizing aerodynamic lenses for single-particle imaging

Author: Nils Roth,Salah Awel,Daniel A. Horke,Jochen Küpper
Publication: Journal of Aerosol Science
Publisher: Elsevier
Date: October 2018

License Number	5514460143418
License date	Mar 22, 2023

Order Details

Type of Use	reuse in a thesis/dissertation
Portion	figures/tables/illustrations
Number of figures/tables/illustrations	1
Format	electronic
Are you the author of this Elsevier article?	No
Will you be translating?	No

About Your Work

Title	Improving Virtual Impactor Performance via Nozzle Optimization
Institution name	University of Minnesota
Expected presentation date	Apr 2023

Licensed Content

Licensed Content Publisher	Elsevier
Licensed Content Publication	Journal of Aerosol Science
Licensed Content Title	Optimizing aerodynamic lenses for single-particle imaging
Licensed Content Author	Nils Roth,Salah Awel,Daniel A. Horke,Jochen Küpper
Licensed Content Date	Oct 1, 2018
Licensed Content Volume	124
Licensed Content Issue	n/a
Licensed Content Pages	13

Additional Data

Portions	Figure 12, d

Tax Details

Publisher Tax ID	98-0397604